Isotope effects on energy transport in the core of ASDEX-Upgrade tokamak plasmas: turbulence measurements and model validation.

P. A. Molina Cabrera,[1, 2, a)] P. Rodriguez-Fernandez,[1] T. Görler,[2] M. Bergmann,[2] K. Höfler,[3, 2] S. S. Denk,[1] R. Bielajew,[1] G. D. Conway,[2] C. Yoo,[1] A. E. White,[1] and the ASDEX Upgrade Team[b)]

[1)] *Plasma Science and Fusion Center, Massachusetts Institute of Technology, Cambridge, Massachusetts, MA 02139, United States of America*

[2)] *Max Planck Institute for Plasma Physics, Boltzmannstr. 2, 85748 Garching, Germany*

[3)] *Physics Department E28, Technical University of Munich, James-Franck-Str. 1, 85748 Garching, Germany*

(*Electronic mail: pedro.molina@epfl.ch)

(Dated: 18 March 2024)

Design and operation of future tokamak fusion reactors using a deuterium-tritium 50:50 mix requires a solid understanding of how energy confinement properties change with ion mass. This study looks at how turbulence and energy transport change in L-mode plasmas in the ASDEX Upgrade tokamak when changing ion species between hydrogen and deuterium. For this purpose, both experimental turbulence measurements and modeling are employed. Local measurements of ion-scale (with wavevector of fluctuations perpendicular to the B-field $k_\perp < 2\,\mathrm{cm}^{-1}$, $k_\perp \rho_s < 0.2$, where ρ_s is the ion sound Larmor radius using the deuterium ion mass) electron temperature fluctuations have been performed in the outer core (normalized toroidal flux $\rho_{Tor} = 0.65 - 0.8$) using a multi-channel correlation electron cyclotron emission diagnostic (CECE). Lower root-mean-square perpendicular fluctuation amplitudes and radial correlation lengths have been measured in hydrogen versus deuterium. Measurements of the cross-phase angle between a normal-incidence reflectometer and an ECE signal were made to infer the cross-phase angle between density and temperature fluctuations. The magnitude of the cross-phase angle was found larger (more out-of-phase) in hydrogen than in deuterium. TRANSP power balance simulations show a larger ion heat flux in hydrogen where the electron-ion heat exchange term is found to play an important role. These experimental observations were used as the basis of a validation study of both quasi-linear gyrofluid TGLF-SAT2 and nonlinear gyrokinetic GENE codes. Linear solvers indicate that, at long wavelengths ($k_\perp \rho_s < 1$), energy transport in the deuterium discharge is dominated by a mixed ion-temperature-gradient (ITG) and trapped-electron mode (TEM) turbulence while in hydrogen transport is exclusively and more strongly driven by ITG turbulence. The Ricci validation metric has been used to quantify the agreement between experiments and simulations taking into account both experimental and simulation uncertainties as well as up to five different observables accross different levels of the primacy hierarchy.

I. INTRODUCTION

The new generation of tokamak fusion reactors aiming to achieve and exceed break-even conditions will operate with a 50:50 mixture of deuterium and tritium fuel to maximize the fusion reaction rate and arrive at reactor-relevant conditions more easily. Successful design and operation of these reactors requires accurate predictive modeling of plasma confinement in mixed ion species plasmas. There is a long history of research on the effects of ion mass on tokamak confinement properties dating back to the early 1990s[1,2]. A recent review article by Weisen[3] addresses the multiple observations over the last three decades. The general experimental observation is that global energy confinement time increases with ion-mass $\tau_E \propto m_i^{0.09-0.47}$ (where m_i refers to the ion-mass)[3] across a wide range of experimental conditions. This positive dependency is found in contrast to the popular 'gyro-Bohm' scaling of heat diffusivity $\chi_{gB} \propto \frac{T_e}{B}\rho_i^*$ (where $\rho_i^* = \rho_i/a$, ρ_i is the ion Larmor radius and a is the device minor radius, with $\rho_i = \sqrt{T_i m_i}/(Z_{\mathrm{eff}} eB)$ where T_i is the ion temperature, Z_{eff} is the effective charge, e is the electron charge, and B the magnetic field). The gyro-Bohm scaling[4][p. 86] leads to a negative dependency of global energy confinement on ion mass $\tau_{E,gB} \propto a^2/\chi_{gB} \propto m_i^{-1/2}$. The disparity between experiments and simple theory - beneficial to energy confinement on deuterium-tritium plasmas - has been termed the *isotope effect*.

Turbulence diagnostics are ideally suited to directly measure local transport properties and can provide unambiguous evidence of the transport response to a changing ion mass. McKee et al.[5] studied the ρ_i^* scaling of density fluctuation properties by scanning the magnetic field in non-dimensionally similar discharges. It was shown that turbulence radial correlation lengths, fluctuation amplitudes, and decorrelation times follow a gyro-Bohm scaling. Hennequin et al.[6] found a similarly good match with gyro-Bohm scaling in density fluctuations over a wider range of scales spanning $k_\perp = 6 - 30\mathrm{cm}^{-1}$ (where $k_\perp$ refers to fluctuations perpendicular to the tokamak's magnetic field). Both of these experiments used the magnetic field to vary ρ_i^*; transport scaling experiments which vary the ion mass to change ρ_i^* are less common. Holzhauer and Dodel[7] reported density fluctuation measurements in deuterium and hydrogen over $k_\perp = 3 - 15\mathrm{cm}^{-1}$ using collective laser-light scattering in the ASDEX tokamak. Density fluctuation amplitudes in deuterium were found to be larger than hydrogen in both the core and near-edge regions of

[a)] Current address: Ecole Polytechnique Fédérale de Lausanne (EPFL), Swiss Plasma Center (SPC), CH-1015 Lausanne, Switzerland

[b)] See author list of U. Stroth et al. 2022 Nucl. Fusion **62** 042006

the plasma.

All of these experiments have studied density fluctuation properties, yet electrostatic fluctuation-driven radial electron heat flux[8] depends not only on fluctuations in electron density but also temperature, potential, as well as their coherency and cross-phase angles. Correlation electron cyclotron emission (CECE) can be used to measure long-wavelength temperature fluctuations [9,10], frequency spectra, and correlation lengths[11]. Deng et al. [12] reported an isotopic dependence of electron temperature fluctuations at mid-radius ($r/a = 0.5$) in the RTP tokamak using a 3D ECE-imaging diagnostic[13]. In direct contrast to the observations in density fluctuations and a gyro-Bohm scaling, Deng et al. found *higher* T_e fluctuation levels in hydrogen over deuterium with a ratio close to the inverse of the ion mass ratio.

This publication aims at unraveling these contrasting observations. It presents recent experiments from the ASDEX Upgrade (AUG)[14] tokamak to study the differences in turbulent electron temperature fluctuations and their effect in energy transport between plasmas with varying ion masses: hydrogen and deuterium. Local measurements of ion-scale ($k_\perp \rho_s < 0.2$ where $\rho_s = \sqrt{T_e/T_i}\rho_i$ is the sound Larmour radius using the deuterium ion mass in the definition of ρ_i. N.B. The deuterium ion mass is used in all further mentions of ρ_s unless otherwise stated) electron temperature fluctuations and density-temperature fluctuation cross-phase have been performed with a correlation electron cyclotron emission (CECE) diagnostic[15,16] and a perpendicular incidence X-mode reflectometer[17] in the outer core ($\rho_{\mathrm{Tor}} = 0.65 - 0.8$, where ρ_{Tor} is a radial coordinate defining contours of constant toroidal flux[18]), low-field side midplane, of ECRH-heated L-mode plasmas.

The present study makes use of these turbulence measurements as the basis of a validation study[19,20] of the quasi-linear Trapped Gyro-Landau Fluid (TGLF-SAT2) [21] and nonlinear gyrokinetic GENE[22] codes. Accurate quantification of the agreement between experiments and simulations requires a careful consideration of the sources of uncertainty on both fronts as well as the place of each observable in the primacy hierarchy[20]. Since there have been many documented cases of fortuitous good agreement between experiment and simulation when using few observables[20], validation efforts should ideally use as many observables as possible across the primacy hierarchy. This study makes use of up to four different observables, two of which consist of fundamental turbulence properties. Lastly, most previous validation efforts have focused exclusively on deuterium plasmas[23,24]. This is the first validation study across different ion-mass plasmas.

The present article is structured as follows. It begins with a description of the plasma conditions and kinetic profile fits in section III. Fluctuation measurements are presented in section IV A. Modeling results follow starting with power balance in section V A. Quasi-linear and non-linear gyrokinetic simulations are then addressed in sections V B and V C. The validation study is then lastly presented in section VI followed by the conclusions.

II. BACKGROUND

The ion mass affects several plasma parameters such as the ion thermal velocity, ion cyclotron frequency, Alfvèn velocity, ion drift velocities, and electron-ion momentum and energy exchange terms[3,25,26]. Experimentally, it has been observed to affect the period of magneto-hydrodynamic (MHD) events such as sawtooth and edge-localized modes[1]. However, a key aspect dominating particle, energy, and momentum transport is how the small-amplitude, high-frequency fluctuations in plasma density, temperature, and potential from drift-wave instabilities[27] respond to changes in ion-mass. These fluctuations have been broadly identified as the major contributor to the anomalously large amount of cross-field energy and particle transport in tokamaks[8,28].

The ion-mass scaling of the energy confinement time can be studied through dimensionless parameter scaling[29,30]. In this approach, the thermal diffusivity can be expressed in the form $\chi = \frac{T_e}{eB}\mathscr{F}(\rho_i^*, \beta, \nu^*, q, T_e/T_i, LX, \text{plasma shape}, ...)$ where $\mathscr{F}$ is a function depending on the normalized ion Larmor radius (ρ_i^*), the ratio of kinetic to magnetic pressures (β), the collisionality (ν^*), safety factor (q), ratio of electron to ion temperatures, gradient scale lengths of density and temperature (LX), and plasma shape - among others[30,31].

Diffusive transport arguments suggest a scaling $\chi \sim (\Delta l)^2/\Delta t$, where Δl stands for the fluctuation's characteristic length scale and Δt for the correlation time. If both Δl and Δt scale with ρ_i[32], then $\mathscr{F} \propto \rho_i^*$ and a gyro-Bohm scaling is obtained. The gyro-Bohm scaling results from fine-scale, collisionless, electrostatic, micro-instability linear drift-wave modes, and it is captured by quasi-linear and non-linear gyrokinetics in the local, electrostatic, collisionless, flowless limit with adiabatic electrons[3]. If Δl scaled instead with $\rho_i^{1/2}$ - as can be the case in linear ion-temperature gradient (ITG) theory in a toroidal geometry[32] - then $\mathscr{F}$ is independant of ρ_i and a Bohm scaling is obtained. The name comes from the empirical Bohm diffusion coefficient, highly successful in describing fully-ionized magnetized laboratory plasmas $\chi_B = \frac{1}{16}\frac{T_e}{eB}$[33][ch.5]. Whether heat transport scales Bohm or gyro-Bohm can have important consequences in the amount of external power required by future burning plasma devices[29,30].

Tokamak experiments feature several ion-mass dependant effects[3,26] that can lead to a reversal of the gyro-Bohm mass scaling. E×B shear stabilization (either via bulk rotation[34] or zonal flows[35,36]), collisional trapped electron mode (TEM) stabilization[37], and electromagnetic effects at high beta [38] are a few examples. Additionally, global full-f gyrokinetic simulations of ITG dominated plasmas have shown the pervasiveness of a Bohm-like ρ_i^* scaling in energy confinement of both electron and ion-heated L-mode plasmas[39]. Recent publications have also highlighted that tokamak edge specific effects (dominated by electron drift-wave turbulence) are also an important part of the puzzle. The non-adiabatic response of fast electron parallel motion[40] as well as edge-specific electromagnetic and collisional effects[41] can exhibit counter gyro-Bohm behaviour.

III. EXPERIMENT DESCRIPTION

Experiments were performed on ASDEX Upgrade[14], a moderate field ($B_T = 2.5$T), medium-sized (major radius $R = 1.65$m, minor radius $a = 0.5$m), tungsten walled, diverted tokamak. The plasma presented in this study is a relatively low density (line average $n_e = 2.5 \times 10^{19}\,\mathrm{m}^{-3}$), electron heated L-mode featuring a plasma current of 1 MA and an on-axis toroidal magnetic field of $B_T = -2.37$ T (where positive is defined as counter-clockwise around the torus looking from the top). An external power of 600 kW is applied using second-harmonic electron cyclotron resonance heating (ECRH) at 140 GHz. This ECRH power is deposited in the plasma core $\rho_{\mathrm{Tor}} < 0.2$. This L-mode reference was first studied in Freethy et al.[24] and has been repeated in both hydrogen (H-36770) and deuterium (D-36974).

It is not possible to perform identical discharges in which the ion mass is changed without affecting many key plasma quantities[3] such as the radial profiles and gradients. In order to attempt relatively similar conditions between isotopes with a limited number of discharges, the strategy was to keep the plasma current, shape, and external power constant and control the core density via active feedback. Electron and ion temperature profiles were allowed to evolve freely. In order to measure temperature fluctuations with low statistical error, the discharges featured a stationary flat-top phase lasting 2.5 s. Figure 1 shows the time traces of key parameters of the two discharges under study. It shows that the core line-averaged density, external ECRH power, and plasma current are well matched. The peak electron temperature is larger in deuterium. Neutral-beam injection (NBI) blips are required to measure kinetic profiles of ion temperature and toroidal rotation velocity. The energy confinement time τ_E is obtained via TRANSP modeling[42] and is calculated by adding the thermal energy contined in electrons and ions and dividing by the power sources (Ohmic and ECRH) minus power sinks (convection, radiation, and charge exchage [43]. $\tau_E$is larger in deuterium than hydrogen, in agreement with the anti-Gyro-Bohm global experimental trends ($\tau_E \propto m^{0.09-0.473}$).

Figure 2 shows average plasma radial profiles during the stationary phase. Electron density is measured using a Thomson-scattering (TS) diagnostic[45], a 5 channel deuterium cyanide (DCN) laser interferometer, and a lithium-beam emission spectroscopy diagnostic[46]. Electron temperature profiles are measured with TS and a calibrated multi-channel electron cyclotron emission radiometer[47]. Ion temperature and toroidal rotation are measured with the charge exchange recombination spectroscopy (CXRS) diagnostic[48]. This diagnostic relies on the charge-exchange reaction between fast neutral particles with carbon or boron impurities in the plasma, and hence it requires either neutral beam injection (NBI) heated plasmas or NBI beam blips. As seen in figure 1, beam blips of 20ms every 300ms are used in these experiments. These short NBI blips do not significantly affect ion temperatures but could induce a finite amount of toroidal torque (i.e. see fig.5 in McDermott et al.[49]). Toroidal rotation profile fits in Fig. 2 (d) take into consideration all data points inside the beam blip and are hence an indicative overestimate of the true intrinsic rotation. The scatter observed in the rotation data did not allow accurate backward extrapolation to obtain true intrinsic rotation as has been done in previous studies[49]. The equilibrium used to map the diagnostics and to perform transport modeling is obtained from the inverse Grad-Shafranov equilibrium solver IDE[50]. It uses pressure profiles and current diffusion modeling to constrain the equilibrium reconstruction[51]. Comparing the IDE equilibrium with the non-kinetic standard CLISTE equilibrium reconstruction leads to differences in mapping of CECE channels in the order of 0.02 in ρ_{Tor}.

Figure 2 and figure 3 show radial profile fits (solid lines) and their logarithmic gradients, respectively. Logarithmic gradient scale lengths are defined as $1/LX = -d/d\rho_{Tor}(\ln(X))$, where X stands for the specific radial profile. Quantitative sensitivity studies[20], as presented in section V B, rely on a robust estimate of the fit, its derivative, and their respective uncertainties. Care has been taken to fit profiles with the latest, most sophisticated, profile-fitting techniques available.

Profile fits for electron density and temperature were obtained using the integrated data analysis (IDA) method[52]. IDA combines several diagnostics within a Bayesian probability framework taking into account the physics and calibration uncertainties of each diagnostic using forward modeling. Since turbulent transport modeling relies critically on accurate profile fits and their uncertainties, the latest IDA algorithm has been employed in this study[51]. It uses a Markov Chain Monte Carlo (MCMC) sampling technique which explores the probability distribution function of a Bayesian data analysis approach which allows a profile estimate from uncertain data input using non-linear forward models. The resulting fit is the mean of the distribution of samples with their standard deviation being the error.

Because of the specific aim of these experiments: validation of turbulence and transport properties, smooth gradients are required. Thus, the number of spline points was decreased to 8 spline knots, roughly half of the usual setting: 19 knots for T_e and 14 knots for n_e. A direct consequence of the reduced spline knots is less variation between samples leading to a smaller estimated error. However, the resulting gradient profiles are within the margin of error of the standard IDA-MCMC and match values obtained with functional fits (i.e. modified hyperbolic tangent function (mtanh[53]) and polynomial spline fits[25]). Ion temperature and toroidal rotation are obtained from a single diagnostic: CXRS. Thus, Gaussian process regression (GPR) has been used to estimate profile fit and gradients[5154]. GPR intrinsically evaluates the fit, its derivative, and their uncertainty, and allows for rigorous uncertainty quantification.

Figure 2 shows that density profiles are well matched, inside error bars, for both isotopes. Electron temperature is larger in deuterium within the range $\rho_{Tor} = 0.2 - 0.8$. Higher T_e in deuterium versus hydrogen was similarly observed for density matched Ohmic L-mode ASDEX experiments[1]. Ion temperature fits show the opposite pattern: a larger ion temperature in hydrogen within the range $\rho_{Tor} = 0 - 0.8$. Toroidal rotation is larger in deuterium than hydrogen and are both positive. Note however that in the region where fluctuation measurements are available, $\rho_{Tor} = 0.65 - 0.8$ (defined as ROI for

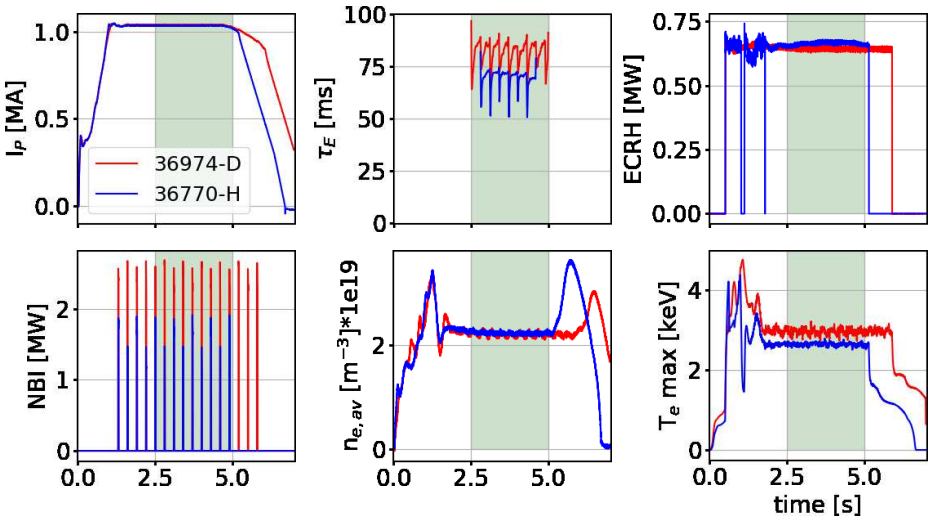

FIG. 1. Reference discharge time trace showing deuterium shot #36974 in red and hydrogen #36770 in blue. The green shaded regions show times used for profile averaging and CECE analysis. Energy confinement times τ_E are obtained via TRANSP modeling[42].

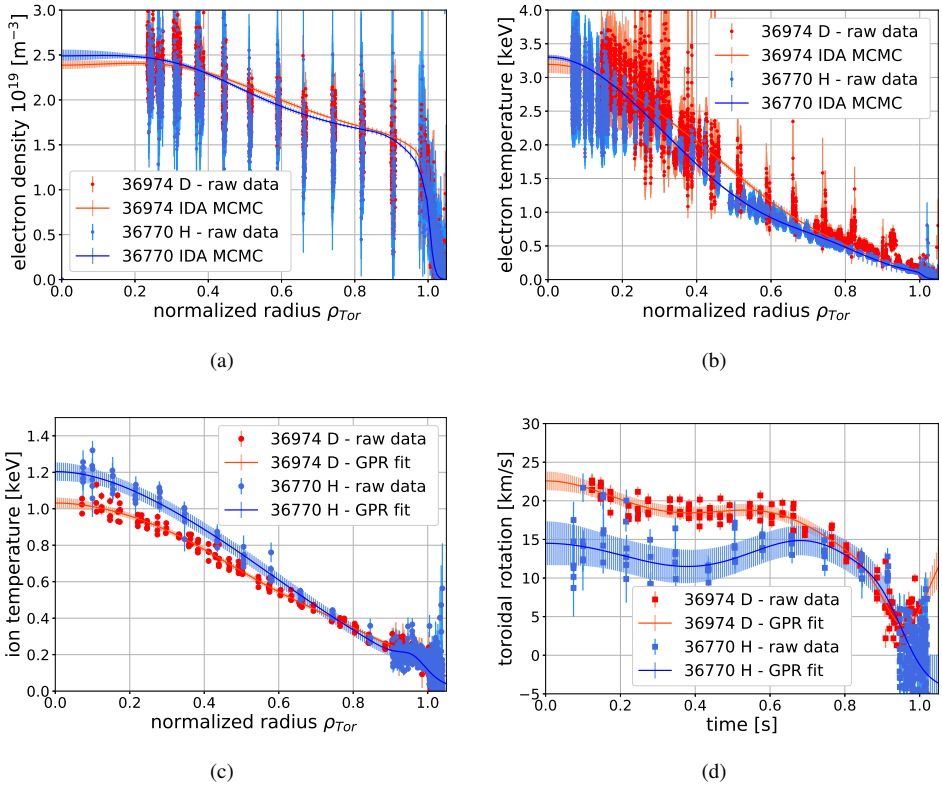

FIG. 2. Radial profiles of (a) electron density (b) electron temperature (c) ion temperature (d) toroidal rotation for deuterium (36974) and hydrogen (36770) in red and blue, respectively. Positive toroidal rotation means counter-clockwise looking down into the torus [44][p. 33]. 1σ error bars are shown in all plots.

region of interest henceforth), all profiles can be found within 2σ errors of each other. Logarithmic gradient scale lengths inside the ROI shown in figure 3 are well matched within uncertainty in the electron density, electron temperature, and toroidal rotation. The only clear difference can be seen in the ion temperature gradient which is larger in H than D; although the difference is just outside of error bars (figure 3(c)).

Doppler backscattering[55,56] (DBS, also known as Doppler reflectometry) has been used to measure the perpendicular rotation velocity of fluctuations ($v_\perp$) in deuterium and hydro-

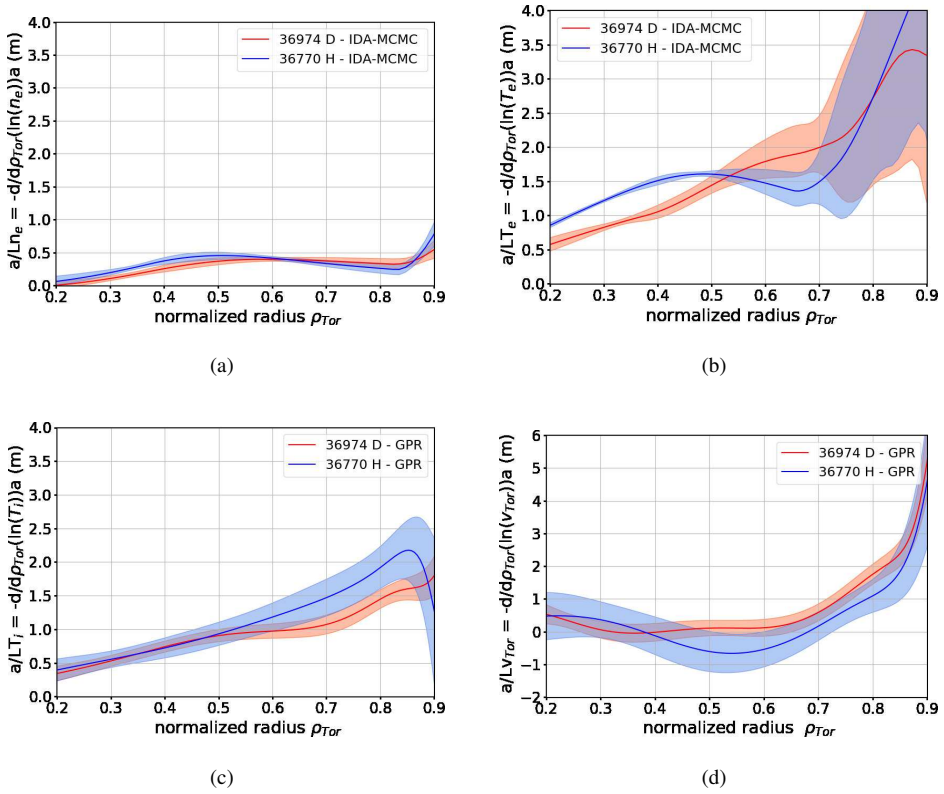

FIG. 3. Logarithmic gradient scale length radial profiles (a) electron density (b) electron temperature (c) ion temperature (d) toroidal velocity for deuterium (36974) and hydrogen (36770) in red and blue, respectively. 1σ error bars are shown in all plots

gen discharges. Perpendicular $\perp$ here refers to normal to the magnetic field. $v_\perp$ is composed both of a plasma background $E\times B$ velocity ($v_{E\times B}$) and a phase velocity of turbulent fluctuations (v_{ph}) components[57]. Figure 4 shows both the scattered signal spectrograms and inferred $v_\perp$ profiles over plasma radius. These measurements reveal that the momentum input of NBI beam-blips (required for CXRS measurements) leads to important changes in $v_\perp$: both in absolute value and profile for both isotopes. The spectrograms in figure 4 show that immediately after the beam blip and for the next $\sim$100 ms, the scattered signal's spectrum shows larger Doppler shift values than $\sim$100 ms before the next beam blip. Figure 4(b) and (d) thus show the $v_\perp$ profiles over plasma radius 100 ms before and after the beam-blip. It appears that the increase in $v_\perp$ is more significant in the deeper in the core $\rho_{Tor} < 0.7$. Regardless of the beam-blip dynamics, figure 4 shows that $v_\perp$ profiles are significantly larger in deuterium ($v_\perp \sim 1.3$ km/s) than hydrogen ($v_\perp \sim 0.3$ km/s) inside the ROI. This stands in contrast to v_{Tor} measurements in figure 2 and is further discussed in section V C.

A spatially constant effective ion charge (Z_{eff}) is estimated using bremsstrahlung radiation in the background CXRS spectra[51]. The deuterium plasma featured an average $Z_{eff} = 1.8 \pm 0.7$ while the hydrogen plasma $Z_{eff} = 1.5 \pm 0.5$. It can be inferred thus, that the hydrogen plasma contains a smaller impurity density which is consistent with bolometer measurements [25,58]. Total radiation power inside the separatrix is $P_{\text{rad-D}} = (405 \pm 40)$ kW in deuterium and $P_{\text{rad-H}} = (353 \pm 25)$ kW in hydrogen. A neutral particle analyzer was used to measure the ratio between hydrogen and the total amount of hydrogen neutral particles - both hydrogen and deuterium- arriving at the plasma periphery. The ratio is less than (5 ± 2) % during the deuterium discharge and (90.6 ± 0.7) % during the hydrogen discharge. These measurements provide confidence that fueling was sufficient and that wall-recycling did not lead to a mixed-species plasmas in either discharge.

Sawtooth frequencies are determined via spectral analysis of core ECE channels to be $f_D^{ST} \approx 0.56$ kHz and $f_H^{ST} \approx 1.2$ kHz. Beam blips are observed to strongly decrease the sawtooth frequency; these estimates were thus taken in-between beam blips when the sawtooth frequency was steady. The smaller deuterium sawtooth frequency is in agreement with an trend reported in ASDEX experiments[1] which observed that the sawtooth frequency scaled as $f_{ST} \propto A_i^{-0.54}$, where A_i is the atomic mass number.

IV. FLUCTUATION MEASUREMENTS

A. Temperature fluctuations

A CECE diagnostic[15,16] was used to measure broadband (<1 MHz), low amplitude (< 2%) electron temperature fluc-

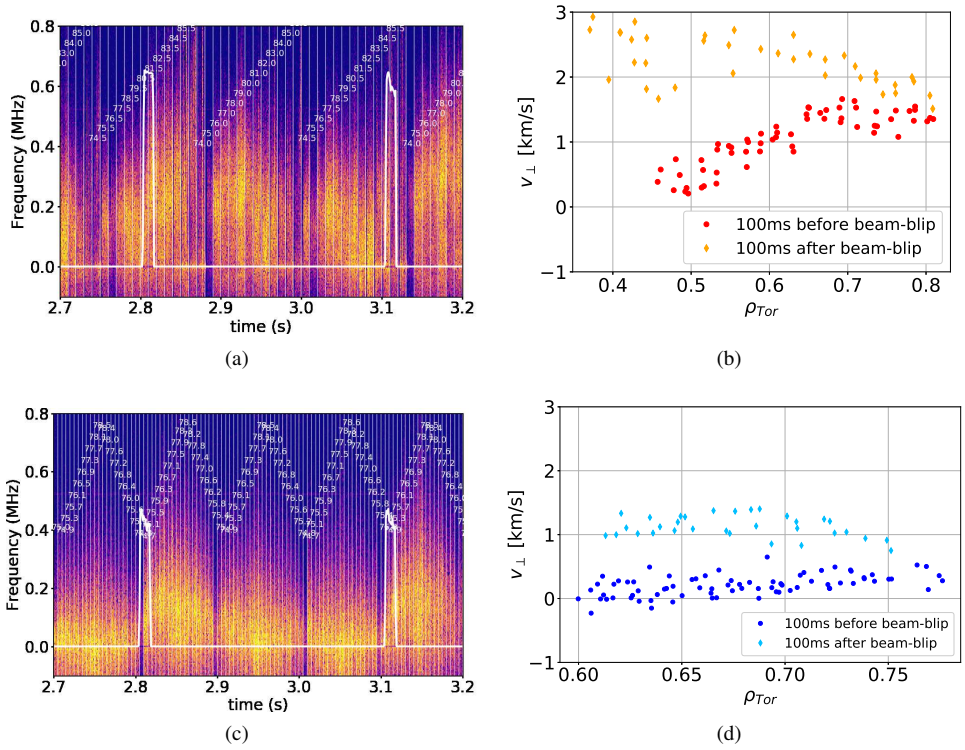

FIG. 4. Figures (a) (deuterium discharge 37974, repeat of 36974) and (c) (hydrogen 38142, repeat of 36770) show the backscattered signal's raw auto-power spectral density time evolution. The stair-case frequency ramps are shown with opaque vertical lines and frequency values in GHz. The NBI beam-blips are superimposed with arbitrary scaling to highlight the strong impact of NBI beam-blip momentum input on the measured Doppler shift and hence $v_\perp$. Figures (b) and (d) show the $v_\perp$ profiles over plasma radius from DBS data both 100ms before and after the NBI beam-blip. The DBS diagnostic was setup to sample at wavenumbers inside $k_\perp \sim$7-8cm^{-1}) in both discharges. Positive rotation in (b) and (d) refers to the ion diamagnetic rotation direction which corresponds to clock-wise rotation in the poloidal plane[44][p. 33].

tuations perpendicular to the magnetic field during both hydrogen and deuterium discharges inside the outer core region $\rho_{Tor} = 0.65 - 0.8$. These small fluctuations have been associated with drift-wave turbulence in tokamaks, believed to be a major contributor to cross-field transport[8,59]. The CECE diagnostic is a heterodyne radiometer operating in F-band between 110 GHz to 125 GHz. The fluctuations observed in the single ECE radiometer signal cannot be interpreted as turbulent temperature fluctuations[60] because of the incoherent nature of black-body electron cyclotron emission in the core of a tokamak and the radiometer detection process[61]. AUG's CECE radiometer uses frequency-domain cross-correlation[62,61] between two radially close-by ECE channels to circumvent the large natural amount of black-body noise in the signal and access small turbulent temperature fluctuations.

AUG's CECE diagnostic features 24 intermediate-frequency (IF) channels which allow the measurement of radial temperature fluctuation frequency spectra dT_e(f) up to 1 MHz bandwidth (anti-aliasing low-pass filter), fluctuation levels (dT_e/T_e), and radial correlation lengths $(L_{r,c}(T_e))$ simultaneously. The frequency spacing between filter center frequencies is 250 MHz, and each channel features a filter with a (200 ± 50) MHz bandwidth. This spacing leads to a separation of about 4 mm to 5 mm in real space and a radial resolution of $\Delta\rho_{Tor} \approx 0.01$ in a typical L-mode plasma. Using a forward-model for ECE radiation transport (the ECRad code[63]), the radial width of the 1/e amplitude of the birth-place distribution of observed intensity[64][p. 21] in the experiments was found to be 5.5 mm at $\rho_{Tor} = 0.75$. Thus, each channel samples a different plasma region radially. In contrast, the $4 - 5$mm radial separation in space is generally smaller than the measured radial correlation length of temperature fluctuations, found in previous studies to be $\sim$10 mm[24]. Hence, two adjacent channels are believed to observe statistically the same fluctuations.

Figure 5 shows the magnitude of the cross-coherence function $|\gamma_{xy}|$[62][p. 32] of three selected pairs of channels in both deuterium and hydrogen discharges. The deuterium spectra show a broad peak in between $20 - 40$kHz which increases in amplitude with radius. The hydrogen discharge shows, in contrast with deuterium, a similar peak but at much lower frequency. This high-frequency broadband feature is often observed in CECE spectra, and it has been associated with drift-wave turbulence [66]. Figure 5 shows an increased level of fluctuations with radius. This is an expected result consistent with previous CECE measurements[66] as well as density fluctuation levels measured with other diagnostics (see for example[5,67]). From the spectra in figure 5, it could be ascertained that, while the limited sampling volume of the CECE diagnostic distorts the real fluctuation spectra and phase velocity, the

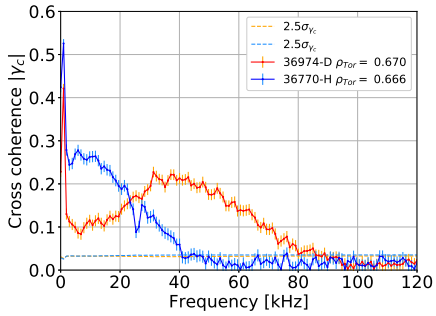

(a)

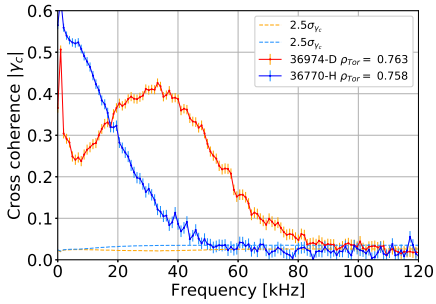

(b)

FIG. 5. Cross-coherence $|\gamma_{xy}(f)|$[62][p. 32] between radially adjacent CECE channels during deuterium (36974 - red) and hydrogen (36770 - blue) discharges showing the frequency dependence of temperature fluctuations with changing radial position: (a) ρ_{Tor} = 0.66 (b) ρ_{Tor} = 0.75. Uncertainty in the coherence and the sensitivity limit (dotted line) are defined in[65].

poloidal rotation velocity of fluctuations is larger in deuterium than hydrogen. It is a well-known fact that drift-wave turbulence propagates perpendicular to the magnetic field[67], nearly normal to the CECE diagnostic line of sight. A larger perpendicular velocity of fluctuations would result in a higher frequency modulation of ECE radiation which in-turn would result in what appears like a larger 'Doppler-shift' of the CECE spectrum. The perpendicular rotation velocity of fluctuations, just as is the case in the DBS diagnostic[57], is combination of the background plasma rotation and the phase velocity of fluctuations. Figure 4 shows that deuterium plasmas do rotate significantly faster ($v_\perp \simeq 1.5\,\mathrm{km\,s^{-1}}$) inside the ROI than their hydrogen counterparts ($v_\perp \simeq 0.3\,\mathrm{km\,s^{-1}}$), a factor of $\times 5-6$. It is important to mention that AUG's CECE line-of-sight featured a 2 deg angle with respect to the normal to the flux surface during this experiments. Thus the changes in the location of the ECE drift-wave feature is believed to be due to modulation of the ECE radiation and not a Doppler shift. GENE simulations presented in section V C further support this assertion.

Figure 6(a) shows the fluctuation amplitude estimate based on the spectra shown in figure 5. The square root of the mean square (rms) of perpendicular temperature fluctuation amplitudes (dT_e/T_e) are estimated using[16]:

$$\frac{dT_e}{T_e} = \sqrt{\frac{2}{B_{IF}} \int_{f_1}^{f_2} \frac{|\gamma_c(f) - \gamma_{bg}|}{1 - |\gamma_c(f) - \gamma_{bg}|} df}, \tag{1}$$

where γ_c and γ_{bg} refer to the complex and background coherence, respectively. B_{IF} is the square root of the product of the intermediate frequency (IF) filter bandwidth of two neighbour channels. f_1 and f_2 refer to the frequency limits within which the drift-wave turbulence pattern is found. This formula is derived in Creely et al.[16] and includes a correction for finite neighbouring IF filter bandwidth overlap through the term γ_{bg}. The magnitude of the complex coherence is taken here instead of only the real part as suggested in Creely et al.[16] in order to consider both real and complex portions of the cross-coherence in the calculation of the total rms fluctuation level. Synthetic diagnostics applied to GENE 2D fluctuation maps (see section V C) reveal that, depending on the line-of-sight, the complex part of the cross-coherence spectra can contain a significant amount of coherence which should be taken into account to compute a total fluctuation level. Taking the absolute value of the complex cross-coherence is also the approach suggested in standard texts such as Bendat and Piersol[62][p. 32]. The integration limits chosen in figure 6 are $5-100$kHz and the γ_{bg} is taken as the average inside $100-120$kHz. In contrast to Creely et al.'s error bar approximation, since γ_c is not much smaller than 1 in this case, the full error propagation formula is used in equation 1 leading to the following expression for the uncertainty (standard deviation) of the rms temperature fluctuation amplitudes ($\sigma_{(dT_e/T_e)}$) in figure 6:

$$\sigma_{(dT_e/T_e)} = \frac{1}{B_{IF}} \frac{1}{dT_e/T_e} \sum_{f_1}^{f_2} \frac{\sigma_{\gamma_c} \Delta f}{[1 - |\gamma_c(f) - \gamma_{bg}|]^2}, \tag{2}$$

where σ_{γ_c} is the square root of the variance (standard deviation) of the cross-coherence spectrum γ_c as derived in the Appendix of Smith et al.[65]. Since γ_{bg} is an average over a flat portion of the γ_c spectrum, errors in γ_{bg} are ignored.

Figure 6 shows that fluctuation amplitudes in deuterium are larger than their hydrogen counterparts, well outside statistical error bars and the statistical limit at $\sim$0.1%. Figure 6 (b) shows the ratio between the rms fluctuation levels in figure 6(a) dT_e/T_e(H) and dT_e/T_e(D). Figure 6 (b) shows that the ratio between the amplitudes in H/D follows an ion Larmor radius H/D ratio inside 2σ error bars.

Figure 7 shows the measured radial correlation lengths ($L_{r,c}$) in both hydrogen and deuterium plasmas over radius. These were obtained by fitting a Gaussian function to the normalized cross-correlation coefficient at zero time delay ($\rho_{xy}(\tau = 0)$)[62] between one fixed channel (denoted x) and 4 to 5 neighbour channels (denoted y) with increasing distance. The radial correlation length is defined here as the radial separation where $\rho_{xy}(\tau = 0)$ drops to 1/e. In order to consider only the temperature fluctuation component of the CECE signal, the following formula is used to access $\rho_{xy}(\tau = 0)$:

$$\rho_{xy}(\tau = 0) = \frac{2 \int (\gamma_{xy}(f) - \gamma_{bg}) df}{B'_{IF} \sqrt{|dT_{e,x}/T_{e,x}|^2 |dT_{e,y}/T_{e,y}|^2}}, \tag{3}$$

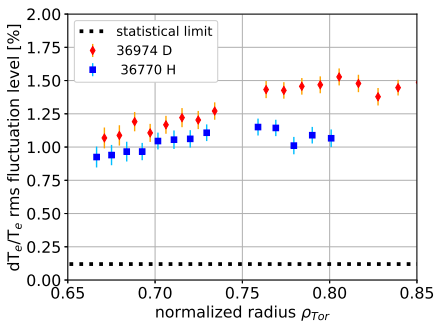

(a)

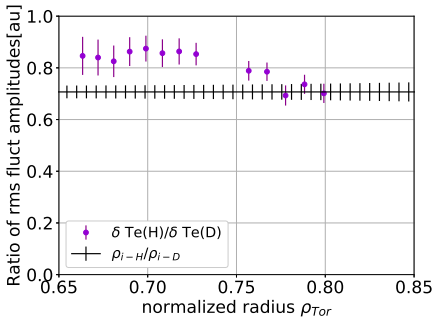

(b)

FIG. 6. (a) Measured perpendicular temperature fluctuation amplitudes in D (36974 - red) and H (36770 - blue) discharges (b) Ratio of hydrogen to deuterium perpendicular temperature fluctuation amplitudes showing that the difference in amplitudes follows a H/D ion Larmor radius ratio.

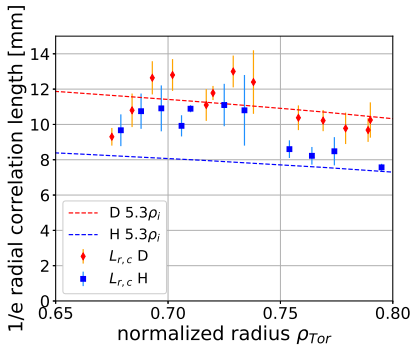

(a)

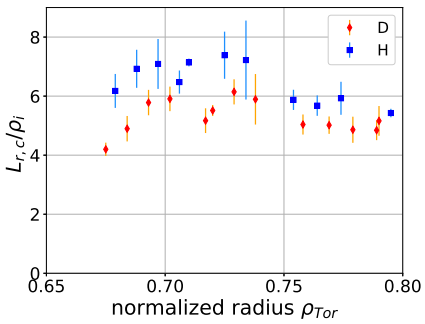

(b)

FIG. 7. (a) Measured radial temperature correlation lengths $L_{r,c}$ in D (36974 - red) and H (36770 - blue) discharges. Gaussian fits were used and 1/e amplitude and 1σ fit erros bars are shown. (b) Ratio of radial correlation lengths in D(red) and H(blue) over their respective ion Larmor radius.

where B'_{IF} is the square root of the product of two IF filter bandwidths (which in this case need not be necessarily neighbours) and $dT_{e,x/y}/T_{e,x/y}$ are the fluctuation levels at the location of a specific channel (an average between fluctuation levels with channels immediately before and after the channel x/y in question). Appendix A shows the full derivation of this formula. While the line-of-sight of the CECE diagnostic is not perfectly normal, it features only a very small angle of $\sim 2^\circ$ with respect to the normal, hence the displacement between channels is essentially radial.

$L_{r,c}$s in both deuterium and hydrogen seem to broadly decrease with increasing plasma radius. Correlation lengths in deuterium are also clearly larger than those in hydrogen, well outside error bars in over 70% of channels. The ion Larmor radius multiplied by an arbitrary constant of 5.5 is plotted with a dotted line in figure 7(a). This Larmor radius scaling seems able to roughly explain both the radial decrease over radius and the difference between the isotopes. Motivated by discussions in [5,68], the correlation lengths of both ions was divided by their respective ion Larmor radius as shown in figure 7 (b). The result is that both ions seem to obey a 5-7ρ_i scaling, roughly independent of ion mass, specially for channels outside $\rho_{Tor} > 0.75$. Figures 6 and 7 demonstrate that a local gyro-Bohm scaling of temperature fluctuations holds in the outer core of these L-mode plasmas in AUG.

B. Beam radius effects

The CECE diagnostic currently uses the mm-wave quasi-optics of AUG's profile ECE system as described by Classen et al.[69]. It uses a 25dB gain D-band rectangular horn antenna which couples to three high-density polyethylene lenses and measures in the low-field side midplane of AUG plasmas. The antenna and RF hardware sit on a rail that can be moved by 60 mm radially and allows the probing beam poloidal waist location to be adjusted. A wire grid selects a vertical polarization in the laboratory frame, which leads to $\approx 2\,\%$ signal losses due to a finite edge B-field pitch of $\approx 11^\circ$ during the L-modes studied here. The electrodynamics reciprocity theorem is used here to assume that the incoherent ECE power coupled into the antenna is well described by the antenna radiation pattern[70].

The finite antenna pattern in the poloidal plane and the limited radial extent of the measured ECE radiation result in an unavoidable limited sampling volume, which leads to biased measurements of turbulence properties[71][ch. 5]. The limited poloidal sampling volume leads to reduced measured fluctuation amplitudes and increased correlation lengths[72]; it acts as a sort of spatial low-pass filter for ion-scale fluctuations in wavenumber space.

It is important to note that the diagnostic beam radius in the poloidal plane is not constant throughout the entire sampling range in figures 6 and 7 shown above. Vacuum complex-beam ray-tracing, also known as Arnaud's method [73], has been used to model the beam properties through the optics system [69]. Since the CECE antenna was placed slightly off-axis due to practical reasons and the beam's size was of the order of the lens' dimensions, traditional Gaussian beam q-parameter calculations[74][ch. 2] are not applicable. Assuming vacuum propagation through the vessel (no plasma), the position of the rail was optimized such that the beam waist was found at ρ_{Tor} =0.75 - close to the middle of the sampling range. At $\rho_{Tor} = 0.75$, the CECE diagnostic filters fluctuations perpendicular to the magnetic field with $k_\perp < 2\text{cm}^{-1}$ ($k_\perp \rho_s < 0.2$) due to its antenna E-field beam radius of ≈7.6 mm. The beam radius varied between 7.8 mm at $\rho_{Tor} = 0.67$ and 14 mm at $\rho_{Tor} = 0.84$. However, as is well-known from experience modeling ECRH beam propagation, the geometric-optics approach used in ray-tracing may not be appropriate inside fusion-relevant plasmas where large gradients can give rise to significant diffraction effects. The TORBEAM code[75] has been used to better quantify diffraction effects, and it has been found that the beam's E-field radius can significantly increase by roughly a factor of ~ 2. TORBEAM predicts the beam radius varied between 27 mm at $\rho_{Tor} = 0.67$ and 19 mm at $\rho_{Tor} = 0.84$. The plasma is sufficiently far from a cutoff that refractive effects have been tested to be in the mm-range. Nonetheless, both ECRad and TORBEAM consider refraction to estimate an accurate ECE emission position.

Due to the finite ECE radial emission width, estimated at ∼5 mm, radial fluctuations are filtered under $k_r < 5\text{cm}^{-1}$ ($k_r \rho_s < 0.5$). Since the toroidal viewing angle is only about 1°, the ECE emission radial size is dominated by relativistic mass-shift broadening[71][p. 165].

Lastly, note that CECE measures predominantly fluctuations perpendicular to the main magnetic field. Due to the much larger conductivity along the magnetic field lines, turbulent structures are highly elongated in the parallel direction ($k_\perp \gg k_\parallel$)[8]. The antenna pattern in the parallel direction ($w_\parallel$) is thus very small in comparison $k_\parallel w_\parallel \ll 1$[72]. The contribution to the experimentally measured fluctuation levels from fluctuations parallel to the field is thus negligible.

C. Density-temperature fluctuation cross-phase angle

Coupling a fluctuation reflectometer[76] (in perpendicular incidence to the cutoff layer, not in the Doppler backscattering[55] configuration) and a ECE radiometer through the same antenna and aligning the reflectometer cutoff and ECE resonance has been used as an attempt to measure the cross-phase angle between density and temperature fluctuations, α_{nT}. This approach was pioneered by Häse et al.[77] in W7-AS and later demonstrated in DIII-D[23,78]. While α_{nT} is not directly responsible for cross-field energy transport[27], it has been shown to respond to changes in experimental gradients and dominant micro-instabilities[79]. In the experiments reported here, a W-band heterodyne system[17] operating in X-mode polarization was used as a fluctuation reflectometer by aligning the antenna in perpendicular incidence to the cut-off and sharing the line-of-sight with the F-band correlation radiometer described above.

Although the reflectometer phase has been most often associated with analytic treatments of the reflectometer signal as density fluctuations[76,80], the reflectometer amplitude has been shown to give a stronger dn_e-dT_e cross-coherence signal with ECE signals experimentally[78]. Furthermore, cross-phase angles between the reflectometer's amplitude and ECE signals were found to be identical to those between reflectometer's phase and ECE signals[78].

Previous experimental results have also shown that the homodyne signal, $A\cos\phi$ (where A and ϕ stand for the reflectometer amplitude and phase, respectively)- which responds linearly with the amplitude A - can measure density fluctuation correlation lengths in agreement with probe diagnostics[81,82]. Two-dimensional full-wave[83] as well as physical-optics[84] simulations attest to the increased reliability of the reflectometer amplitude over the phase signal to access radial correlation lengths. However, most studies used cross-correlations between reflectometer channels and do not address directly under which conditions the fluctuation reflectometer's amplitude and/or phase signal by itself is a valid kernel of density fluctuations.

There can be adverse experimental conditions, termed the non-linear regime, which lead to large localization uncertainty[85]. Using heat-flux matched gyrokinetic simulations presented in section V C, density fluctuation level dn_e/n_e and radial correlation lengths can be approximated as 0.5 % and 10 mm. These can be used as input to the criteria for the non-linear regime presented by Gusakov and Popov[85] as $\gamma = (\omega/c)^2 l_{cx} x_c (dn_{e,rms}/n_c)^2 \ln(x_c/l_{cx}) \geq 1$, where l_{cx} is the radial correlation length of turbulence, x_c is the cut-off distance from the plasma edge (∼8 cm here), n_c is the density at the cut-off layer, $dn_{e,rms}$ is the rms value of density fluctuations, and ω is the sampling frequency. The regime in this experiments is thus *linear* since $\gamma \approx 0.1$. This implies that the reflected signal's amplitude and phase are mostly coming from the cutoff region[85].

Recent simulation results have cast doubt as to whether the reflectometer-amplitude signal is an unbiased kernel of density fluctuations. It has been shown that there may be a cross-phase angle between density fluctuations and the reflectometer-amplitude signal depending on linearity, the radial turbulent wavelength spectrum, and the sampling beam radius of curvature[86]. While these results are from a conference proceeding and have not been peer-reviewed, they are a clear warning that the accurate interpretation of the experimental cross-phase measurements between reflectometer-amplitude and ECE signals requires careful modeling. Full-wave modeling is beyond the scope of this work. Yet, it is deemed interesting to present experimental cross-phase measurements nonetheless.

Figure 8 shows both the magnitude of the complex cross-coherence and cross-phase spectra between the W-band reflectometer-amplitude signal and a single CECE channel

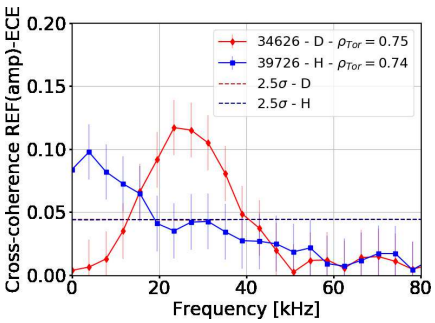

(a)

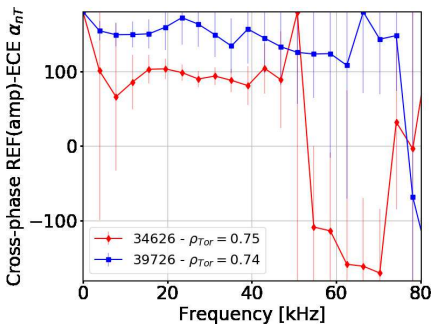

(b)

FIG. 8. (a) Absolute value of complex cross-coherence $|\gamma_c|$ spectrum and (b) Cross-phase spectrum between reflectometer amplitude and ECE radiometer signal in both deuterium (34626-red) and hydrogen (39726-blue) discharges. Reflectometer frequency was 75GHz in 34626 and 76GHz for 39726. The radiometer frequencies have been used to localize the measurement as shown in the legend. Discharges 39726 and 36974 were successful repeats of 36770 and 34626, respectively, with identical machine settings.

signal during deuterium (34626) and hydrogen (39726) discharges. These discharges are repeats of 36974 and 36770 presented above. The reflectometer frequency and CECE channel positioning were chosen to find a cross-phase angle around $\rho_T = 0.75$ to agree with the location of simulations presented below. In discharge 34626, the magnitude of the cross-coherence was largest at precisely $\rho_T = 0.75$ as shown in figure 8. For 39726, the peak cross-coherence was found in a deeper channel ($\rho_T = 0.7$), but the statistically-significant cross-phase angle found on this channel was identical to that observed in $\rho_T = 0.74$ as reported in figure 8. The reflectometer amplitude signal has been chosen because cross-correlation with the reflectometer phase led to significantly lower cross-coherence: below the 2.5σ level, and thus not statistically significant.

The cross-phase angle is found to change with isotope mass, outside of error bars. On average, inside the region of significant coherence ($|\gamma_c| > 2.5\sigma$), $\alpha_{\text{RefA-ECE}} = 100 \pm 16^\circ$ in deuterium and $153 \pm 20^\circ$ in hydrogen. Experimental error bars come from the root sum square of the statistical variance of the cross-power phase spectrum[65] and the standard deviation of the cross-phase inside the region of significant coherence. In both discharges, the cross-phase angle is positive: the reflectometer-amplitude signal *leads* the ECE signal.

Previous results from DIII-D have reported a negative cross-phase angle between the reflectometer-amplitude and ECE signals[23,78]. Freethy et al.[24] in AUG also reported a negative cross-phase angle; however, the cross-phase definition was changed to be between the ECE radiometer and the reflectometer-amplitude signals (see equation 2 in[24]). The cross-phase results presented in figure 8 are the result of a cross-power spectral density computation[62][p.335] between density (x) and temperature (y) fluctuation kernels:

$$\begin{aligned} \alpha_{\text{xy}} &= \tan^{-1}(Q_{xy}/C_{xy}), \\ G_{xy} &= \frac{2h}{N}|X_k^* Y_k|, \\ G_{xy} &= C_{xy} - iQ_{xy}, \end{aligned} \tag{4}$$

where N is the number of samples, h is the sampling period, Y_k is the Fourier transform of signal $y(t)$ and X_k^* is the complex conjugate of X_k. The reflectometer amplitude signal is used as the kernel for density fluctuations (x) while a temperature trace (a positive growing signal with increasing plasma temperature) is used as the kernel for temperature flucutuations (y).

Previous studies have highlighted that cross-phase magnitudes moving towards zero are consistent with an increased trapped-electron mode (TEM) drive in the non-linear turbulence mix[79]. Since $|\alpha_{\text{RefA-ECE}}(\text{H})| > |\alpha_{\text{RefA-ECE}}(\text{D})|$, it can be similarly hypothesized, experimentally, that there is a stronger electron turbulence drive in the deuterium discharge turbulence mix. This hypothesis is consistent with the increased ion temperature gradient (LT_i) in figure 3 (c), which drives a stronger ion turbulence mix in the hydrogen discharge.

V. TRANSPORT MODELING

A. Interpretative power balance

The TRANSP code[42] is used to empirically interpret transport features of both H and D discharges. TRANSP is a 1.5D equilibrium and transport solver[87]. It uses a fluid description of the plasma to solve magnetic field diffusion as well as particle, momentum, and energy conservation equations. Figure 9 shows the inferred *power balance* electron and ion heat fluxes. These definitions follow transport equations in Braginskii[88].

The input density and temperature profiles are shown above in section III. The kinetic IDE equilibrium is used to define the simulation domain and boundaries. The Kadomtsev model[89] is used to ensure that the effects of sawteeth in the current density - and hence in the Ohmic power - are taken into consideration. Measured Z_{eff} and bolometry radiation radial profiles are additional inputs. Figure 9 shows error bars in heat fluxes. These were obtained by running 25 separate TRANSP simulations varying input uncertainties within $\pm 2\sigma$ based on the specific uncertainties of all input profiles: n_e,

T_e, T_i, P_{rad}, and Z_{eff}. The input uncertainties were Gaussian-distributed and featured a mean around zero and a standard-deviation of 1σ. At $\rho_{Tor} = 0.73$, the standard deviation of the resulting heat fluxes was 18 % and 23 % for the electron and ion heat flux, respectively.

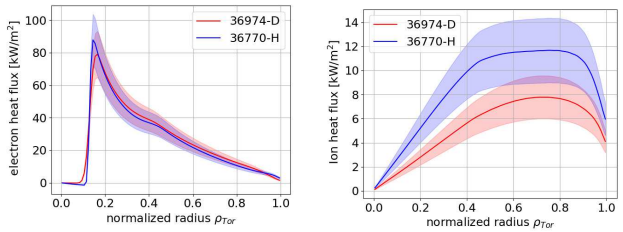

(a) (b)

FIG. 9. Average radial profiles of (a) electron and (b) ion heat flux [kW/m^2] output from the TRANSP power balance calculation. Note that the y-axis scaling is not the same and $Q_e \gg Q_i$ for most of the radius.

The mean electron heat flux is larger in deuterium than hydrogen by about ∼20 %, but it lies well inside error bars in the ROI ($\rho_{Tor} = 0.65 - 0.8$). The opposite is seen in the ion heat flux where Q_i in H is larger than D by about ∼60 %. This difference is larger than the difference in electron heat flux, but it is still inside 1σ error bars in the ROI. However, for most of the deep core $\rho_{Tor} < 0.5$, the ion heat flux is larger in H than D outside of error bars.

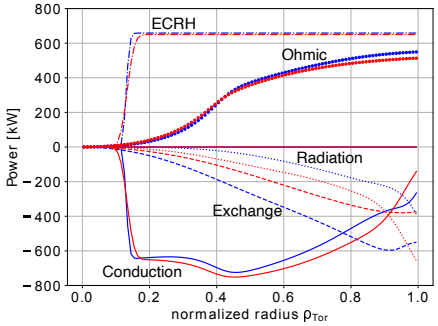

FIG. 10. Electron power balance terms during discharges 36974-D (red) and 36770-H (blue).

The electron power-balance terms are plotted for both D and H discharges in figure 10. This figure shows that there are small variations in many quantities in the power balance: ECRH power, radiation and Ohmic power. These are caused by the difference in Z_{eff}, radiation, and input profiles shown in section III. However, the most important difference between both discharges is the electron-ion heat exchange term, analytically evaluated as[88]:

$$\begin{aligned} p_{ei} &= \frac{3m_e}{m_i}\frac{n_e}{\tau_e}(T_e - T_i) \\ &= \frac{4e^4\sqrt{2\pi m_e}\log\Lambda}{m_i}\frac{Z_{eff}n_e^2}{T_e^{3/2}}(T_e - T_i), \end{aligned} \tag{5}$$

where $\log\Lambda$ is the Coulomb logarithm and τ_e is the electron-ion collision characteristic time. Figure 11 shows the radial dependence of the ratios of various terms in p_{ei} which can change between discharges: $T_e - T_i$, $1/T_e^{3/2}$, Z_{eff}, n_e^2, and the inverse ion-mass $1/m_i$. Density and Z_{eff} ratios remain close to one for most of the plasma radius. In contrast, the T_e-T_i, $1/T_e^{3/2}$ terms can vary from near 1 in the deep core to 0.5 and ∼1.5 at $\rho_{Tor} = 0.6$. The p_{ei}(H)/p_{ei}(D) ratio is then dominated by the inverse ion-mass term in the deep core. This inverse ion-mass term highlights that electron energy is more easily coupled into the colder ions via Coulomb collisions for the lighter hydrogen ions. However, at $\rho_{Tor} = 0.6$, the difference in temperatures can also become important and the p_{ei}(H)/p_{ei}(D) ratio reaches only about 1.3. Therefore, it is observed that the ion-mass dependence of the electron-ion heat exchange term explains the differences in power balance terms inside $\rho_{Tor} < 0.5$. Yet, temperature profile differences can become important further outside. The role of the ion mass was presented by Schneider et al.[25], although in a much higher density discharge and hence in a different collisionality regime. The present experiments confirm that at almost half the core density, the mass dependence of the electron-ion heat exchange term still has an important effect on the power balance of AUG L-modes.

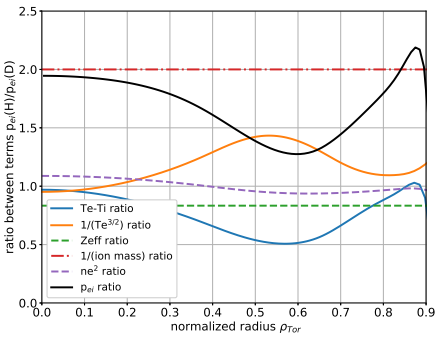

FIG. 11. Ratios between terms in the electron-ion heat exchange term between hydrogen and deuterium discharges.

Inside the ROI, heat diffusivities are very close between both isotopes. Electron heat diffusivities are about $\chi_e \approx 1.5 - 2\mathrm{m}^2\mathrm{s}^{-1}$, very similar for both ions. Ion heat diffusivities are larger in hydrogen than deuterium but well inside error bars between $\chi_i = 2 - 3\mathrm{m}^2\mathrm{s}^{-1}$. Smaller profile error bars are required to arrive at relevant empirical evidence of any isotope effects in heat diffusivities in the ROI. It appears, nonetheless, that heat diffusivity hints at a Bohm-like scaling of transport which could be due to ρ_i^* effects as suggested by Idomura[39]. Simulations[90] showed that ρ_i^* effects were important from $1/\rho_i^*$ 150 to 600 which include the $1/\rho_i^* \sim 550$ range of the present experiments.

B. Gyro-Landau fluid modeling via TGLF

The trapped-gyro-Landau fluid (TGLF) code has been used to model and describe the turbulent energy transport of the discharges above. TGLF uses the trapped-gyro-landau-fluid equations[91] to provide an accurate approximation to the linear eigenmodes of tokamak drift-wave instabilities. The resulting eigenmodes are then used to compute quasi-linear energy fluxes. The quasi-linear approach uses a saturated turbulence intensity model based on a large set of non-linear gyrokinetic turbulence simulations[92]. The latest and most accurate non-linear saturation rule, SAT2[93] , has been employed in this study. This new saturation rule includes the full 3D dependence (poloidal angle, radial and poloidal wavenumber) of the saturated electrostatic potential fluctuation intensity. It has been verified and calibrated against a database of CGYRO turbulence simulations[94].

TGLF uses the spectral shift method[95] to account for $E \times B$ shear suppression of turbulence. It calculates the $E \times B$ shear rate[96] from TRANSP estimates of the radial electric field E_r invoking radial force balance, neoclassical estimates of poloidal rotation, and experimental toroidal rotation input.

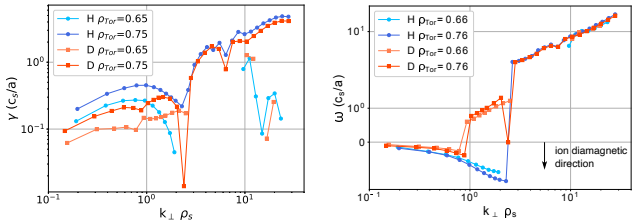

(a) (b)

FIG. 12. TGLF SAT2 dominant mode results for nominal gradient input at $\rho_{Tor} = 0.66$ and $\rho_{Tor} = 0.76$ in deuterium and hydrogen discharges: (a) Linear growth rates (b) Real frequency spectra. Ion diamagnetic direction corresponds to negative frequencies as shown by the arrow.

Figure 12 shows the dominant mode linear growth rates and real frequency spectra obtained from TGLF using nominal profile inputs. Nominal refers to simulations that use the original profile fit gradients and Z_{eff} values from experiment. These plots are normalized by c_s/a where c_s is the electron sound speed: $c_s = \sqrt{T_e/m_D}$ and a is the plasma minor radius. Discharge-specific temperature profile and a constant deuterium ion mass are used in this normalization to meaningfully compare growth rates. Figure 12 shows that both shots feature unstable ion temperature gradient (ITG) modes propagating in the ion-diamagnetic direction at long-wavelengths $k_\perp \rho_s < 1$. Growth rates are larger at $\rho_{Tor} = 0.76$ than at 0.66 in both isotopes as can be expected from mixing length arguments given the increased profile gradients with increasing radius. Furthermore, dominant-mode linear growth rates under $k_\perp \rho_s < 0.2$ appear larger in hydrogen. Since these plasmas are ITG dominated, this increase in H over D could be due to the higher ion temperature gradient in the ROI $\rho_{Tor} = 0.65 - 0.8$ as shown in figure 3(c).

TGLF calculates a normalized temperature fluctuation intensity spectrum in wavenumber space ($A_{\text{tot}}(k_y)$ where k_y stands for $\text{k}_\perp \rho_s$ with $\rho_s = \sqrt{T_e m_i}/(Z_{\text{eff}} eB)$) which can be used to compare with experimental CECE measurements. It accounts for fluctuations driven by both dominant and subdominant modes as follows:

$$A^2_{\text{tot}}(\text{k}_y) = \sqrt{\sum_{\text{m=modes}} A^2_m(\text{k}_y)} = \frac{a}{\rho_s}\frac{d}{d\text{k}_y}\left(\left|\frac{dT_{e,\text{tot}}(\text{k}_y)}{T_e}\right|^2\right),$$

where $(A^2_m(\text{k}_y))$ are the fluctuations driven by a given mode, a is the minor radius, and $dT_{e,\text{tot}}(\text{k}_y)/T_e$ is the total temperature fluctuation in frequency-wavenumber space given by TGLF. In order to recover the total temperature fluctuation level from the fluctuation intensity, an integral in the wavenumber space is required to invert the above equation. A quantitatively correct comparison with temperature fluctuation measurements performed via CECE requires a physically sound synthetic weight function in wavenumber space $(W(\text{k}_y))$ to be included in the wavenumber integral as follows:

$$\left|\frac{dT_{e,\text{tot}}}{T_e}\right| = \sqrt{\frac{\rho_s}{a}\int_{\text{k}_y} W(\text{k}_y)\cdot A^2_{\text{tot}}(\text{k}_y)d\text{k}_y}.$$

Previous synthetic diagnostics have used box-car weight functions[97] for $W(\text{k}_y)$, which can only be considered approximate and do not reflect the Gaussian spatial distribution of a mm-wave antenna pattern. A new weight function $W(\text{k}_y)$ is proposed here which consists of a spatial Fourier transform of a Gaussian beam in real space as first suggested by Bravenec et al.[72]:

$$\frac{dT_{e,\text{m}}(\vec{\text{k}},\omega)}{T_e} = e^{-(\vec{\text{k}}\cdot\vec{d}/2)^2}\frac{dT_{e,\text{tot}}(\vec{\text{k}},\omega)}{T_e},$$

where $dT_{e,\text{m}}(\vec{\text{k}},\omega)/T_e$ and $dT_{e,\text{tot}}(\vec{\text{k}},\omega)/T_e$ are the square root of the measured and total temperature fluctuation temporal-spatial spectral power density, respectively. $\vec{d}$ is a 3D vector representing the sampling volume. Since TGLF solves for fluctuations localized at a particular radial location and because turbulent structures in a tokamak are elongated along the toroidal dimension ($\text{k}_\perp \gg \text{k}_\parallel$), the $\vec{\text{k}}\cdot\vec{d}$ term can be simplified to $\text{k}_{\text{vert}}\cdot d_{\text{vert}}$, where vert stands for the vertical dimension in the laboratory and d_{vert} stands for the sampling 1/e-amplitude beam radius. Note that the relevant d_{vert} in this case does not correspond to the standard 1/e-amplitude of the electric field beam radius, w, used to describe millimeter-wave quasi-optical beams in standard textbooks[74][ch.2]) but should correspond to the 1/e *power* beam radius: a $\sqrt{2}$ scaling factor is required $d_{\text{vert}} = w/\sqrt{2}$. Thus, the weight function becomes:

$$W(\text{k}_y) = e^{-\frac{k_y\cdot w}{\sqrt{2}}}$$

Figure 13(a) shows TGLF's raw temperature fluctuating intensity and weight functions for the case of the hydrogen discharge at $\rho_{Tor} = 0.75$ using nominal input gradients.

Linear interpolation is used to increase the $k_\perp$ resolution of the wavenumber integral. There are cases, as shown in figure 13(a), where the fluctuation amplitude at the first $k_\perp$ is non-zero. Since TGLF does not provide a solution at $k_\perp$=0, the first $k_\perp$'s A^2 value is assigned for $A^2(k_\perp = 0)$. This choice is based on GENE simulations where the temperature fluctuation k-spectra showed a non-zero amplitude at $k_\perp = 0$ due to zonal (radial) components excited via nonlinear coupling.

Before comparing TGLF temperature fluctuation measurements with experimental CECE measurements, two additional corrections were required. First, the magnetic reconstruction was used to find the local magnetic field pitch angle at the measurement locations which corresponded to $\sim 11^\circ$. The cosine of this angle was taken to account for the projection of the vertical antenna pattern in the $k_\perp$ space defined by TGLF. Secondly, as shown in Görler et al.[98], temperature fluctuations may have quite anisotropic components parallel and perpendicular to the main field. The TGLF fluctuation intensity $A^2_{\text{tot}}(k_y)$, accounts for the total fluctuation level, while CECE measures predominantly the perpendicular component[72](see section IV A). Since exclusively perpendicular temperature fluctuations could not be extracted from TGLF, a factor of 30% scaling factor has been applied in this study $dT_{e,\perp} \approx 1.3 dT_{e,\text{Total}}$ based on GENE simulations[98] at $\rho_{Tor} = 0.75$ as shown in section V C.

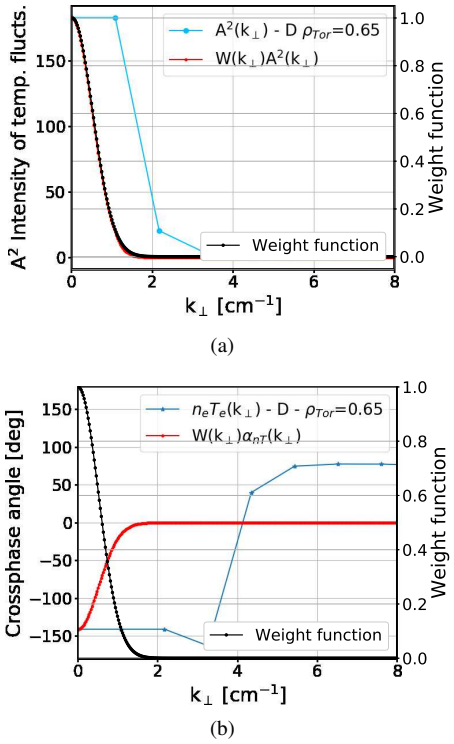

FIG. 13. TGLF synthetic diagnostic details: (a) TGLF temperature fluctuation intensity wavenumber spectrum and weight function used to estimate a single-valued synthetic dT_e/T_e level and compare with experiments. (b) TGLF nT cross-phase wavenumber spectrum and weight function used to estimate a single-valued synthetic α_{nT} cross-phase angle to compare with experiments.

TGLF also calculates the quasi-linear cross-phase angle between density and temperature fluctuations in wavenumber space, which can be compared with experimental measurements. The Gaussian weight function developed above can be used in a simple weighted average to extract a single-valued synthetic TGLF α_{nT} estimate. This approach ignores the spatial properties of the reflectometer antenna pattern and takes exclusively the sampling volume of the ECE radiometer. This is justified on the basis that the spatial volume common to both diagnostics is limited by the smallest footprint between the two[99]. Since both use the same line of sight, the relevant volume is limited by the ECE radiometer antenna pattern which is the smallest of the two because of its higher microwave receiver frequencies. Figure 13(b) shows a sample nT k-spectrum and the weight function. Inside the relevant wavenumber range covered by the Gaussian weight function, the nT cross-phase is found negative. It disagrees with the positive sign of the experimental cross-phase measurements between the reflectometer amplitude and the ECE radiometer as presented in seection IV A. However, the absolute value of the nT cross-phase angle seems to be close to experiments $\sim$100-150°.

Prior to comparing turbulence simulations with experiment, a 'base' case is sought in order to ensure that the heat fluxes are in agreement with experiment and the turbulence state represents experimental conditions. Thanks to the speed of TGLF simulations and the availability of local fluctuation data, the Validation via Iterative Training of Active Learning Surrogates (VITALS) [100] framework was used. VITALS exploits surrogate-based strategies using Gaussian processes and sequential parameter updates to achieve the combination of plasma parameters that best matches experimental transport measurements within diagnostic error bars. In this paper the VITALS framework is used to vary the input uncertainties of logarithmic gradients (Ln_e, LT_e, LT_i), $E \times B$ shear rate ($\omega_{E\times B}$), and Z_{eff} in an attempt to find the best match to experimental output electron and ion heat fluxes as well as turbulence properties: CECE temperature fluctuation levels and nT cross-phases.

Figure 14 shows both nominal and VITALS results and how much they disagree in percentage with the experimental values. Nominal results provide a look into how discrepancies in heat fluxes are linked to discrepancies in turbulence properties and serve as a useful contrast with VITALS 'base-case' results.

The first striking feature of figure 14 is that ion heat fluxes (Q_i) are strongly overestimated; factors of $\times 4-7$ are observed in nominal simulations while factors of $\times 2-4$ are seen in VITALS simulations. While VITALS clearly brings Q_i towards agreement, the discrepancies are maintained well outside 2σ error bars. In contrast, electron heat flux (Q_e) is much better estimated. Nominal simulations also overestimate Q_e but only by factors between $\times 1.5-2$. VITALS successfully brings Q_e to within 1σ error-bar agreement, with the only exception of hydrogen at $\rho_{Tor} = 0.75$. Temperature fluctuation levels (dT_e/T_e where the subscript $\perp$ denoting perpendicular to the field has been dropped for convenience) as well as the absolute values of density-temperature cross-phase an-

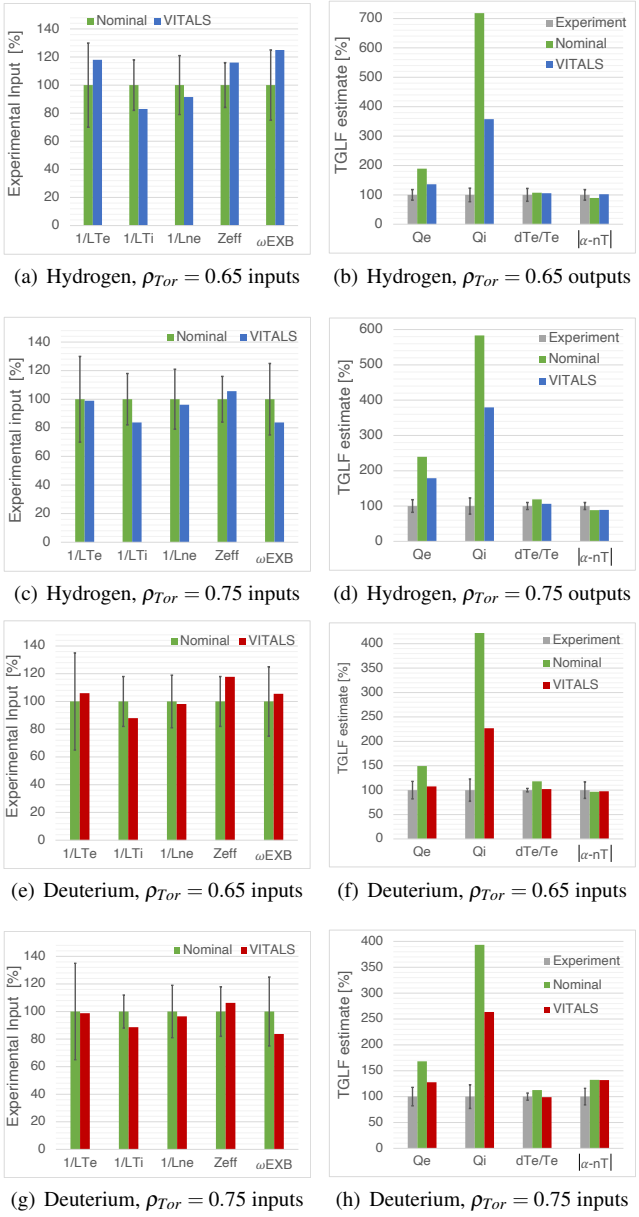

(a) Hydrogen, $\rho_{Tor} = 0.65$ inputs (b) Hydrogen, $\rho_{Tor} = 0.65$ outputs

(c) Hydrogen, $\rho_{Tor} = 0.75$ inputs (d) Hydrogen, $\rho_{Tor} = 0.75$ outputs

(e) Deuterium, $\rho_{Tor} = 0.65$ inputs (f) Deuterium, $\rho_{Tor} = 0.65$ inputs

(g) Deuterium, $\rho_{Tor} = 0.75$ inputs (h) Deuterium, $\rho_{Tor} = 0.75$ inputs

FIG. 14. Summary of TGLF simulation results. Left-hand side figures show the nominal (green) and VITALS (blue for hydrogen and red for deuterium) inputs to TGLF along with experimental error bars for inputs. Right-hand side figures show the output of both nominal and VITALS simulations and how these compare with experimental results (gray) which feature appropriate experimental error bars.

gles ($|\alpha_{nT}|$) are found in relative good agreement in nominal simulations already. VITALS brings both quantities towards closer agreement with experiment and agreement within 1σ is found except for $|\alpha_{nT}|$ at $\rho_{Tor} = 0.75$ in deuterium. TGLF does recover successfully the experimental pattern observed in figure 6, namely, larger dT_e/T_e in deuterium than hydrogen. $|\alpha_{nT}|$ is found in agreement within 2.5 σ error in most cases, but does not change significantly between isotopes and thus does not recover the pattern observed in figure 8.

In summary, varying input gradients, $v_{E\times B}$ shear, and Z_{eff} within 1σ errors allows for a good match of electron heat flux Q_e and dT_e/T_e. While the α_{nT} cross-phase angle is negative in all simulations, its absolute value seems to be in the same ball-park as experimental measurements. However $|\alpha_{nT}|$ in the simulations fails to change significantly with isotope mass. Ion-heat fluxes are found to be consistently overpredicted in both isotopes, particularly strongly in the case of hydrogen. These results encourage a revision of the quasi-linear saturation rules in different isotopes and/or a reconsideration of experimental T_i radial profiles and LT_i gradients in both isotopes. Section VI B below attempts to quantify the agreement between experiments and TGLF simulations.

C. Gyrokinetic modeling via GENE

The Eulerian nonlinear gyrokinetic code GENE[22] has been used to further understand the turbulent transport in this pair of discharges and to compare turbulence measurements with state-of-the-art gyrokinetic modeling[98,101].

These simulations include electromagnetic effects, collisions modeled with a linearized Landau operator, and employ a field-line tracing algorithm to obtain the flux surface shape and metric from the kinetic IDE equilibrium reconstruction. Furthermore, external $E \times B$ shear flow and parallel flow shear effects are retained in nonlinear simulations. By default, the main ions and electrons are considered as active gyrokinetic species with the actual mass ratios. The Z_{eff} value is either considered in two-species simulations as a corresponding rescaling of the ion-electron collisionality or used to derive the density of a third gyrokinetic species by assuming fully ionized boron impurities with density gradients, temperature and its gradient taken from the main ion species (with density of the latter accordingly reduced).A summary of the physics inputs is shown in table VIII in Appendix B.

Firstly, the GENE linear solver was used to hint at the most important micro-instability dominating turbulent transport in these discharges. Figure 15 shows the linear growth rate of nominal-input case scenarios in both hydrogen and deuterium. Scans of input gradients and Z_{eff} (inside 1σ) are included to hint at the possibility of mixed turbulence drives inside experimental input error bars. In the case of hydrogen, regardless of input changes to gradients and/or Z_{eff} all linear growth rates at low-k propagate in the ion-diamagnetic direction. In the case of deuterium, however, there are cases where an increased electron temperature gradient and/or density gradient can turn the lowest part of the spectrum into a dominant electron mode, very likely trapped-electron-mode (TEM) at such low-k. Additionally, contrasting hydrogen and deuterium growth rates in figure 15 shows that, inside ion-scales, the linear growth rates in hydrogen are larger than in deuterium. This is similar to what was observed in TGLF growth rates in figure 12(a). Again, the larger ion temperature gradient in the hydrogen discharge could be contributing to stronger ITG growth-rates.

Non-linear gyrokinetic simulations have also been performed at $\rho_{Tor} = 0.75$. These are ion-scale, local (flux-tube) simulations. A synthetic diagnostic has been employed to quantitatively compare non-linear GENE simulation outputs

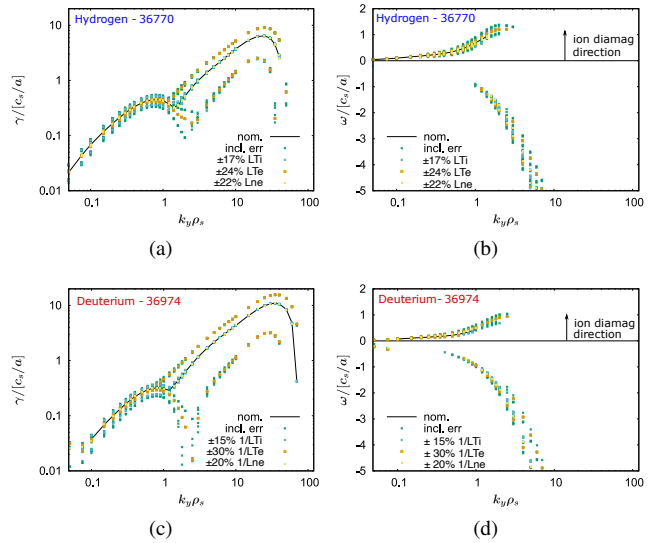

FIG. 15. Linear growth rate and mode frequency for both hydrogen (a and b) and deuterium (c and d) discharges performed at ρ_{Tor} =0.75. 1σ scans of input gradients and Z_{eff} are included to hint at the possibility of mixed linear turbulence drives. Omti, omte, and omn stand for input gradient scale lengths of ion temperature, electron temperature, and density, respectively. The percentages varied correspond to the uncertainty presented in section III.

with experimental data. GENE's field-aligned fluctuating quantities can be mapped into a 2D space in lab-coordinates where experimental sampling volumes can be directly applied to mimic experimental measurements with great fidelity. Since the CECE diagnostic would predominantly measure the perpendicular component of temperature fluctuations due to its antenna pattern, the perpendicular component of temperature fluctuations is extracted from GENE simulations[98] to compare with experiment. A 'point spread function' (PSF) after Holland et al.[101] is used to model the effect of finite diagnostic sampling volume on the measured turbulence properties[72]. The PSF consists of a 2D Gaussian with anisotropic radial and vertical dimensions. Using a forward-model for ECE radiation transport (the ECRad code[63]), the *radial* 1/e amplitude of the birth-place distribution of observed intensity[64][p. 21] was found to be 5.5 mm at $\rho_{Tor} = 0.75$. The *vertical* 1/e-amplitude of the electric field beam radius (w) was obtained using complex-beam ray-tracing through the optics and TORBEAM inside the plasmas as outlined in section IV B. Just as done in the TGLF synthetic diagnostic above, since the CECE measures ECE *power*, the power beam radius $w_{\text{Pow}} = w/\sqrt{2}$ is used in the GENE PSF. The GENE synthetic diagnostic has been implemented in Python[24] and has been numerically verified to provide identical results to previous implementations in IDL[98,101].

Figure 16 compares perpendicular temperature fluctuation frequency spectra from GENE and experiment in both hydrogen and deuterium plasmas. Both figures feature 'nominal' and 'best' synthetic GENE traces which stand for simulations performed with the original input gradients and those where the best overall match of heat-flux and turbulence quantities has been found. The 'best' simulations are the result of an empirical 15-simulation scan of input gradients and Z_{eff} within 1σ experimental errors. These 'best' match simulations were also found when using a third gyrokinetic species to model Z_{eff} in both hydrogen and deuterium simulations. The large computation time required for convergence of these non-linear simulations did not allow a thorough scan of input parameters and/or the use of a VITALS-like tool as in the case of TGLF (see section V B). However, the TGLF-VITALS results informed the gradient quantities to be modified towards a better agreement with experiment.

Note that the y-axis of the plots in figure 16 are not in arbitrary units but in physical relative fluctuation amplitude squared $(dT_e/T_e)^2$ per kHz; neither the experimental data nor the simulation's synthetic diagnostic output have been scaled relative to each other. The physically correct scaling is obtained using the cross-power spectral density (CPSD) algorithm found in Bendat and Piersol[62][p.301-327]. Hann windows are used for spectral leakage and set to 50 % overlap for frequency-domain averaging. In order to reproduce the experimental conditions as accurately as possible, time traces from two separate channels featuring the diagnostic line-of-sight and inter-channel separation are used in the cross-power calculation. The synthetic CPSD was initially found to feature many oscillations due to the short time periods of 2D turbulence data from the GENE simulation, lasting only about $1-2$ms. In order to reduce this scatter, PSF time-traces from 5 pairs of volumes placed before and after the simulation point were used to arrive at the mean cross-power trace in figure 16. Since flux-tube non-linear GENE simulations were run using local profile information at $\rho_T = 0.75$, the turbulence conditions in the neighbouring channels are believed to be identical. The error bars in the synthetic spectra are the standard deviation of the mean.

The experimental dT_e/T_e frequency spectrum from CECE data is taken from the integrand in equation 1 (see section IV A). This is because the CECE radiometer is not absolutely calibrated and because cross-talk can occur between filters, requiring the active subtraction of the background coherence. Nonetheless, the same CPSD algorithm is used to compute experimental and synthetic GENE frequency spectra. Equation 2 is used for the experimental error bars, which appear relatively small in figure 16 due to the large number of data points acquired during a 2.5-second flat-top phase at 4MHz sampling.

Figure 16 (a) shows GENE synthetic dT_e/T_e spectra in comparison with experimental CECE results in deuterium. Figure 16 (a) contrasts the effects of using different models to estimate the vertical antenna pattern. Using complex-beam ray-tracing leads to significantly smaller ($\times 2-3$) vertical beam radii when compared with TORBEAM results (see section IV B). Using the same GENE simulation output, the vertical sampling dimension was changed between vacuum complex ray-tracing and TORBEAM estimates. A narrower beam radius selects a larger portion of the k-space, and hence leads to a larger dT_e/T_e fluctuation level. Figure 16(a) shows that the vacuum estimate contains fluctuations in agreement with experiment inside $5-50$kHz, but it also features signifi-

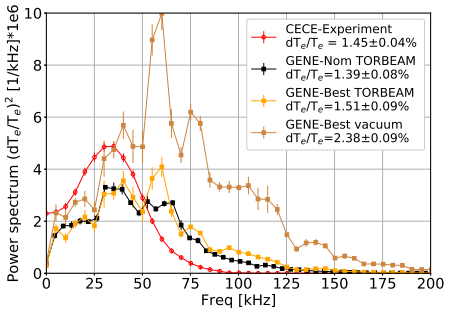

(a)

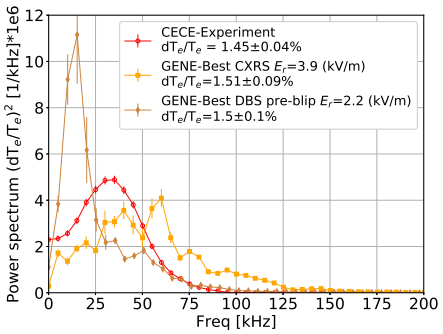

(b)

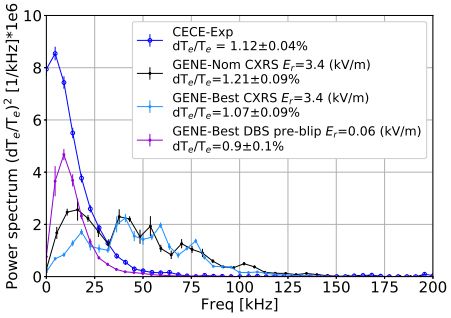

(c)

FIG. 16. Comparison of synthetic (GENE) and experimental (CECE) temperature fluctuation spectra in (a,b) deuterium and (c) hydrogen. dT_e/T_e fluctuation level estimates result from integrating the spectra inside 5-125kHz. (a) shows the effect that the synthetic vertical beam radius has on the dT_e/T_e spectra and level. (b) and (c) show the effect that using E_r estimates from CXRS and DBS has on the dT_e/T_e spectra and level.

cantly more power in higher frequencies which is not seen in experiment. The integrated dT_e/T_e spectrum over all frequencies leads to an overestimate of the total fluctuation level when compared with CECE data. Using the TORBEAM w_Z estimates results in a slight underestimate when compared with the experimental observations, but the integrated $dT_e/T_e(f)$ can be found in better agreement with experiment, inside 1σ error bars. The better agreement between TORBEAM-GENE and CECE data provides confidence that the TORBEAM beam radius is likely a better estimate of the beam radius in experiments. In all future observables presented in this paper, the TORBEAM beam-radius estimate will be used.

Figure 16 (b) and (c) contrast the effects of background plasma $E\times B$ rotation on the shape of the resulting synthetic CECE spectrum. Section III, in particular figures 2d and 4, showed that while the toroidal rotation measured via CXRS was similar (within error bars), the perpendicular rotation of turbulent fluctuations showed an important $(\times 5-6)$ difference between deuterium and hydrogen at ρ_{Tor} =0.75. Plasma flow shear can significantly influence turbulent transport. GENE flux-tube simulations employ an $E\times B$ shear model first suggested by Hammett et al.[102] and later improved by McMillan et al.[103]. GENE simulations use the radial force balance equation to compute the input E_r profile[104][p. 61],[105]:

$$E_r = \frac{\nabla p_\alpha}{Z_{\text{eff}} e n_\alpha} - \mathrm{v}_{Pol} B_{Tor} + \mathrm{v}_{Tor} B_{Pol} \tag{6}$$

where α refers to any plasma species. Due to its choice of field-aligned coordinates, GENE is currently limited to considering shear flow effects along the toroidal direction, i.e. the toroidal velocity shear. This is typically considered a reasonable assumption for core plasma simulations where the $\mathrm{v}_{Tor}B_{Pol}$ term is thought to dominate the radial force balance equation 6. Simulations with an artificial $\mathrm{v}_{Tor} = E_r/B_{Pol}$ can be made to investigate the effect of changing $E\times B$ flow amplitude.

AUG's CXRS diagnostic measures light emitted from boron impurities, thus E_r can be found directly from measured boron density gradients, temperatures, and toroidal rotation together with the IDE magnetic reconstruction. The poloidal rotation can be either inferred from asymmetries in toroidal rotation[106] or calculated from neo-classical estimates. In the case of the discharges studied here, poloidal rotation estimates were only available inside $\rho_{Tor} < 0.5$, thus, the code NCLASS(CAR48)[107] was used to estimate $\mathrm{v}_{Pol}(D) = 0.3$ and $\mathrm{v}_{Pol}(H) = 0.25$ $\mathrm{km\,s^{-1}}$ at ρ_{Tor} =0.75. Lebschy[105][p. 84] showed that neoclassical poloidal rotation estimates were in agreement within error bars with poloidal rotation measurements in typical AUG L-mode plasmas inside $\rho_{Tor} = 0.7-0.8$. Table I shows the estimates of E_r from CXRS. The uncertainty in these estimates was calculated via uncertainty propagation taking: profile errors as shown in figures 2 and 3, a 20% error on the boron density profile gradient, a poloidal rotation uncertainty of $\sigma \mathrm{v}_{Pol} = 0.2\mathrm{km\,s^{-1}}$[105], and no error in the magnetic reconstruction.

Another instrument that can be used to infer E_r is DBS. It measures the perpendicular rotation of turbulent fluctuations which is composed both of the plasma's $E\times B$ rotation velocity and the phase velocity v_{ph} of fluctuations. The radial electric field can thus be obtained:

$$E_r = (\mathrm{v}_\perp - \mathrm{v}_{ph})B \tag{7}$$

where B is the total magnetic field. The phase velocity can be estimated from linear GENE simulations shown in figure 15 taking $\mathrm{k}_y = \mathrm{k}_\perp = 7\mathrm{cm}^{-1}$ as chosen in experiments. The phase velocities are found to be $\mathrm{v}_{ph} = \omega/\mathrm{k}_y \simeq 0.43\rho_s\frac{c_s}{a} \simeq 0.22\,\mathrm{km/s}$ and $\mathrm{v}_{ph} \simeq 0.57\rho_s\frac{c_s}{a} \simeq 0.27\,\mathrm{km/s}$ for deuterium and

hydrogen, respectively. E_r estimates from DBS using measured $v_\perp$s both 100 ms before and after the NBI beam blip are reported in table I. Uncertainties are calculated via error propagation taking the spread of $v_\perp$ velocities shown in figure 4 as $\sigma_{v_\perp} \sim 0.2\,\mathrm{km/s}$ and the variation in $\sigma_{\omega/(c_s/a)} \simeq 0.3$ with changing input gradients (see figure 15) as $\sigma_{v_{ph}} \sim 0.14\,\mathrm{km/s}$.

Diagnostic	E_r(kV/m) 36974 Deuterium	E_r(kV/m) 36770 Hydrogen
CXRS	3.9±1.1	3.4 ± 1.2
DBS (post beam-blip)	3.1±0.2	1.3 ± 0.2
DBS (pre beam-blip)	2.2±0.2	0.06 ± 0.2

TABLE I. Estimates of radial electric field E_r from CXRS and DBS diagnostics at ρ_{Tor} =0.75 in both deuterium and hydrogen discharges.

Table I shows that the estimates from CXRS and DBS (post beam-blip) agree inside $1-\sigma$ errors in deuterium but only inside $1.5-\sigma$ in hydrogen. It also shows that taking DBS data well away (200ms) from the NBI beam-blip, the E_r estimate can change significantly - well outside error bars. Since NBI beam-blips are known to input momentum to the plasma[49] and since CXRS measures the toroidal rotation during the beam-blip exclusively, it is safe to argue that CXRS E_r estimates are biased and likely overestimate the $E \times B$ rotation. Furthermore, since CXRS E_r estimates feature the highest amount of uncertainty, the DBS pre beam-blip E_r estimates are believed to be the most reliable to represent the background $E \times B$ rotation.

Figures 16(b) and 16(c) show the effect of using either the CXRS or DBS pre beam-blip E_r estimates on the shape of the synthetic CECE spectrum and how these compare with experiments. The most salient feature on both isotopes is that a larger E_r leads to a synthetic CECE spectra peaking at higher frequencies. These figures thus furthermore support the hypothesis proposed in section IV A that differences in plasma rotation perpendicular to the CECE line-of-sight lead to changes in the dT_e/T_e frequency spectra shape as shown in figure 5.

Figure 16 (b) shows that the simulation using CXRS's E_r estimate leads to a broad spectrum featuring power in frequencies above 50 kHz, which is not found in experiments. On the other hand, the 'GENE-Best' simulations in figure 16(b) featuring the DBS pre-blip E_r features fluctuations peaking in a frequency range about 20 kHz, underneath that of experiments. In the case of hydrogen, shown in figure 16(c), the CXRS E_r simulations show a much broader spectrum than experiments featuring significant amounts of power in frequencies above 30 kHz. The DBS pre-blip E_r estimates bring the synthetic dT_e/T_e spectrum into much better agreement with experiments.

It must be noted that only the local value of E_r was changed in these flux-tube simulations at ρ_{Tor} =0.75. Changing only the E_r amplitude had no measurable impact (beyond random error) on heat fluxes nor turbulence observable quantities - such as dT_e/T_e. The $E \times B$ shearing rate is calculated from equation 6 using the CXRS input v_{Tor}, ignoring the first two terms in equation 6 as is done by default in GENE core simulations. CXRS and DBS E_r simulations in figures 16(b) and 16(c) only explore the changes of E_r amplitude on the synthetic CECE diagnostic spectrum. Future work could attempt to calculate radial profiles of fluctuation phase velocity and measure radial profiles of poloidal rotation accross the ROI. These would allow to consistently explore the effects of both E_r amplitude and its shear on turbulent energy transport.

Temperature fluctuation level estimates from GENE and experiment are also shown in figure 16. The GENE-best estimates reproduce the experimental observation that dT_e/T_e fluctuation levels are smaller in hydrogen than deuterium. The ratio $dT_e/T_e(\mathrm{H})/dT_e/T_e(\mathrm{D})$ from the GENE-best estimates is 0.77 ± 0.16 compared to the CECE estimate of 0.76 ± 0.14. GENE-estimated dT_e/T_e fluctuation levels, thus, agree with a gyro-Bohm scaling picture suggested in section IV A.

Figure 17 shows the synthetic GENE estimates of the radial correlation length compared with experiment. The synthetic radial correlation length from GENE is determined by calculating the normalized cross-correlation coefficient $\rho_{xy,\Delta r}$ between one fixed channel and neighbour channels with increasing separation.

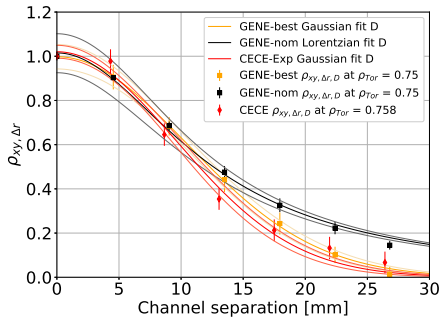

(a)

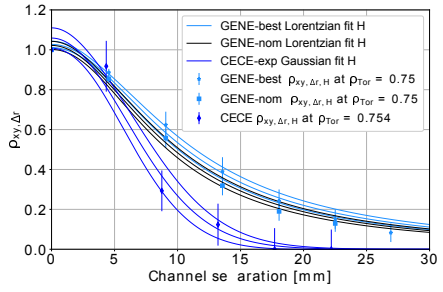

(b)

FIG. 17. Comparison of synthetic and experimental radial temperature fluctuation correlation lengths (a) deuterium (b) hydrogen. CECE-Exp. D Gaussian fit in red features a χ^2=0.96 and a HWHM of 11.4±0.5mm. GENE-best D Gaussian fit in orange features a χ^2=0.5 and a HWHM of 12.3±0.4mm. GENE-nominal D Lorentzian fit in black features a χ^2=1.4 and a HWHM of 12.6±0.3mm. CECE-Exp. H Gaussian fit in navy blue features a χ^2=0.4 and a HWHM of 7.3±0.8mm. GENE-best H Lorentzian fit in light blue features a χ^2=0.7 and a HWHM of 10.7±0.6. GENE-nominal H Lorentzian fit in black features a χ^2=0.8 and a HWHM of 9.7±0.5.

Since the synthetic GENE PSF time traces do not contain any background radiometer black-body noise and provide dT_e/T_e traces, $\rho_{xy,\Delta r}$ can be computed directly using cross-correlation functions at zero time-delay, namely $\rho_{xy,\Delta r} = R_{xy}(\tau=0)/\sqrt{R_{xx}(\tau=0)R_{yy}(\tau=0)}$. The roundabout FFT approach is used to compute these, following Bendat and Piersol[62][p.328-333]. Given the limited duration of the time traces, averaging is performed to minimize the effect of numerical uncertainty on the final fit. This averaging consists of calculating $\rho_{xy,\Delta r}$ for six different inter-channel separations both increasing and decreasing in major radius across the line-of-sight. This process is performed for a central channel aligned with the measurement location at $\rho_{Tor} = 0.75$ and 3 central points both above and below in major radius. The uncertainty is found from the standard deviation of the mean at each inter-channel separation. Experimental CECE $\rho_{xy,\Delta r}$s are found using equation 3 as derived in Appendix A. This equation allows an uncalibrated radiometer to access physically equivalent $\rho_{xy,\Delta r}$s. Experimental error bars come from applying the error propagation formula on equation 3.

The fitting technique and the estimate of fit errors (confidence intervals) are central to a proper quantitative comparison between experiment and synthetic GENE results. CECE experimental $\rho_{xy,\Delta r}$ can be fit by a Gaussian function. The reduced chi-square statistic (χ^2)[108][p. 63-65] is used to quantify the goodness of fit. CECE Gaussian fits in figure 17 feature $\chi^2 = 0.96$ and $\chi^2 = 0.4$ for D and H, respectively. Since both of these χ^2s are close to the ideal 1.0, it can be ascertained that the Gaussian function matches the experimental data in accordance with the experimental uncertainty. On the other hand, the synthetic GENE $\rho_{xy,\Delta r}$s are found to decrease less sharply over inter-channel distance and a Gaussian function leads to $\chi^2 \gg 1$. Instead, a Lorentzian function ($F_L(x) = \gamma A_o/(x^2+\gamma^2)$) is used in these cases, which leads to $\chi^2 \sim 0.7-1.7$. Evaluating the fit confidence interval is a subtle matter prone to underprediction when using least-square optimization. To ensure numerically accurate errors on the fit parameters are obtained, the Bootstrap method was used[109]. It uses a Monte-Carlo algorithm which prepares a large number of different input data sets ($\sim$400) where each data point features normal-distributed random amounts of error inside experimental uncertainty. The least-square fit algorithm is then run independently on these data sets. The sample mean of the bootstrapped parameter estimates is taken as the final fit, and the standard deviation of the output data set as the error bars - plotted in figure 17.

One salient, puzzling, feature of figure 17 is that the synthetic GENE best heat-flux match $\rho_{xy,\Delta r}$ decays just like the CECE experimental data with a Gaussian function, but the hydrogen GENE best heat-flux match $\rho_{xy,\Delta r}$ features 'tails' best fit by Lorentzian instead of a Gaussian function. The reason behind this discrepancy is not clear. Furthermore, half width at half maximum (HWHM) estimates in deuterium seem to agree between GENE and experiment. However, hydrogen GENE $L_{r,c}$ overestimate experimental findings. Moreover, figure 17 also shows that the synthetic GENE correlation length is larger in D than H, reproducing the experimental finding that $L_{r,c}$(D)$>$ $L_{r,c}$(H). The CECE ratio $L_{r,c}$(H)/$L_{r,c}$(D)$=0.68\pm0.09$ agrees roughly inside 2σ error against the GENE ratio $L_{r,c}$(H)/$L_{r,c}$(D)$=0.81\pm0.09$. A gyro-Bohm scaling of $L_{r,c} \propto 1/\sqrt{m}$ is thus reproduced by GENE, within error.

Lastly, figure 18 shows a comparison between the experimental and synthetic-GENE nT cross-phase angles. The GENE cross-phase angle is obtained via equation 4 where the kernels for density and temperature fluctuations are the fluctuating density and perpendicular temperature traces from the 2D GENE synthetic diagnostic. A single PSF is applied to both density and temperature fluctuation maps: identical physical locations and PSF functions are used for both dn_e and dT_e maps. This is justified in the basis that the reflectometer airy width and vertical beam radius are both expected to be larger than their respective ECE emission sizes, and thus the smaller volume of the two is taken[78]. In order to reduce random noise error due to the short duration of synthetic GENE time-traces, the synthetic cross-phase corresponds to the mean from 5 volumes placed before and after the measurement location at $\rho_{Tor} = 0.75$ along the experimental line-of-sight. The error bars in the synthetic spectra are the standard deviation of the mean. Figure 18 shows that GENE, in agreement with TGLF results presented above, also predicts a *negative nT* cross-phase angle. This is found in contrast with the experimental cross-phase angle between the reflectometer's amplitude and ECE signals, which was found positive (see section IV A).

Figure 18 shows that - in the case of both isotopes - if the experimental α_{nT} undergoes a sign reversal, the crossphase angle is found relatively close with GENE synthetic estimates. In the case of hydrogen, the negative of the experimental cross-phase angle agrees within error bars. In deuterium, the angle differs by $\sim30^\circ$, yet agrees inside 2σ error bars. In short, while the nT cross-phase angle of GENE synthetic diagnostics and experimental results do not agree in sign, their amplitude $|\alpha_{nT}|$ is found to be in agreement. Another interesting result found in figure 18 is that the synthetic GENE cross-phase angle is higher in amplitude in H than D, recovering the experimental trend observed. The higher amplitude and more out-of-phase cross-phase angle in hydrogen is consistent with the stronger, unambiguous, ITG drive observed in the linear GENE simulations in figure 15.

The effect of toroidal rotation on the synthetic nT crossphase was found to be very important. Reversing the input rotation direction lead to a sign reversal in the nT crossphase while the magnitude was left unchanged. The negative angle reported here results from a careful transformation of CXRS toroidal rotation profiles (see figure 2) into GENE coordinates.

Figure 19 brings all these observations together and compares inputs and outputs of nominal and 'best-match' simulations of both isotopes. These figures use percentages to highlight how much each quantity was varied in the input and how the non-linear GENE simulations responded to these inputs. 1σ experimental uncertainty in both inputs and outputs is also shown. Two main observations can be made. First, nominal gradient inputs lead to a strong overestimation of the ion heat flux (Q_i) for both isotopes, specially for hydrogen with a $\times3$ overestimate. This can be expected from the hypersensitivity

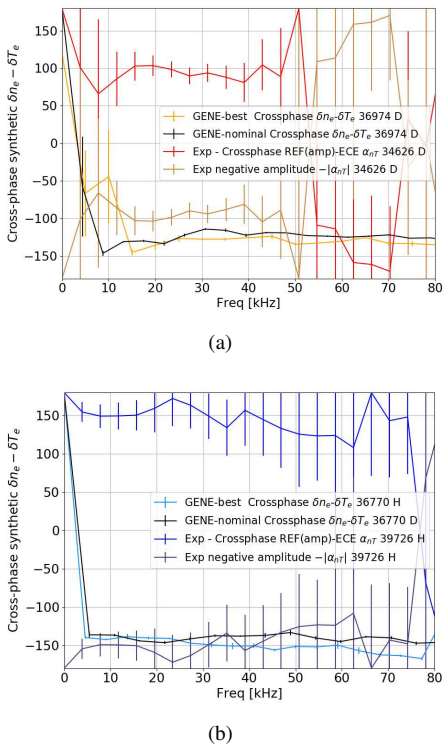

FIG. 18. Comparison of synthetic and experimental dn_e-dT_e cross-phase angle (a) deuterium and (b) hydrogen.

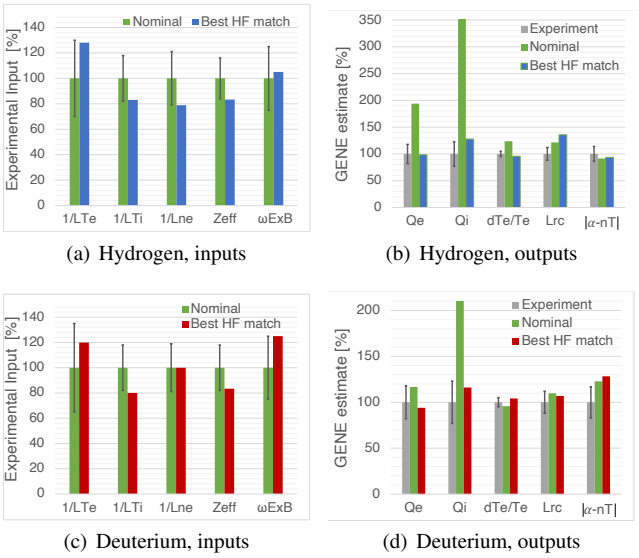

FIG. 19. Summary of GENE simulations and synthetic diagnostic output when compared with experimental results at $\rho_{Tor} = 0.75$. (a) and (c) show inputs to nominal and best heat-flux match simulations in hydrogen and deuterium. (b) and (d) show GENE output compared in percentages with experimental results.

of non-linear simulations to input gradients[110]. The overestimation is not as strong as that seen in the TGLF results in figure 14. It is surprising to see that the turbulent properties do not react significantly to the strong Q_i overestimate, specially the nT cross-phase angle which is supposed to address directly the turbulence mix. Varying input gradients and Z_{eff} within uncertainty, the best-heat flux match simulations succeed in bringing heat fluxes down to within 1σ error, yet a significant change towards agreement is not observed in the turbulence properties tracked in this study (see nT cross-phase in deuterium, for instance). Second, the electron heat flux is well matched by nominal deuterium simulations. Turbulence properties of the nominal deuterium simulation are then also found within 1.5σ error of experiment, which supports the fact that electron heat transport has been well modeled by nominal input parameters. This is not the case for the hydrogen nominal simulations which show an overestimate of Q_e, dT_e/T_e, and $L_{r,c}$. Best heat-flux match hydrogen simulations succeed in bringing the electron heat flux down and also bring dT_e/T_e into 1σ agreement with experiment. However, the $L_{r,c}$ is seen to increase further away from experiment while the $|\alpha_{n,T}|$ changes by a negligible amount. This observation highlights the importance of having many experimental observables in experiment-modeling comparisons since agreement with one quantity can prove fortuitous. It also introduces the need for a composite validation metric which quantifies the agreement between experiment and simulation across multiple observables, as discussed in section VI below.

VI. MODEL VALIDATION

A. The Ricci validation metric

Meaningful comparisons between experiment and simulation require a systematic and quantitative approach discussed in many recent publications[19,20,111]. The Ricci parameter[112] will be used in this study to quantify the experiment-simulation agreement. It makes use of simple mathematical expressions that bring together many observables into a composite metric for agreement χ_R and an overall quality of comparison Q. These two quantities take into consideration experimental and modeling uncertainties as well as the location of the observables inside the primacy hierarchy[20]. These metrics are defined as follows[112]:

$$
\begin{aligned}
d_j &= \sqrt{\frac{(x_j - y_j)^2}{\Delta x_j^2 + \Delta y_j^2}}, \\
R_j &= \frac{\tanh[(d_j - d_o)/\lambda] + 1}{2}, \\
S_j &= \exp\left(-\frac{\Delta x_j + \Delta y_j}{|x_j| + |y_j|}\right), \\
H_j &= 1/h_j,
\end{aligned}
\quad \rightarrow \quad
\begin{aligned}
Q_R &= \sum_j H_j S_j, \\
\chi_R &= \frac{\sum_j R_j H_j S_j}{\sum_j H_j S_j},
\end{aligned}
$$

where j stands for observable, x for experimental measurements, y for modeling results, $\Delta x/\Delta y$ for their respective uncertainties, and h_j for the primacy hierarchy level[20]. The variable d quantifies the difference or distance between experiments and simulation and is normalized by the amplitude square of the respective uncertainties. The variable R uses *'d'*

to quantify the level of agreement between each observable with 0 for perfect agreement and 1 for perfect disagreement. λ and d_o are arbitrary constants that determine the sharpness of tanh transition between 0 and 1. H quantifies the position of the observable in the primacy hierarchy. S quantifies the precision of the measurement with more accurate measurements having a S closer to 1. The composite quantity Q_R combines the precision S and hierarchy H of all observables to quantify the *quality* of the comparison. A higher Q_R implies a more meaningful, better, comparison. Finally, χ_R performs a weighted-sum of the level of agreement R with the quality of each observable to arrive at a final composite metric for agreement between the experiment and the simulation. $\chi_R = 0$ implies perfect agreement while $\chi_R = 1$ implies perfect disagreement.

The hierarchy position of each observable is now addressed. The temperature fluctuation level dT_e/T_e is considered to be *first* in the primacy hierarchy since it comes directly from the integration of the cross-coherence of two nearby radiometer channels and does not require any other diagnostic for evaluation. The radial correlation length $L_{r,c}$ of temperature fluctuations is also considered *first* in the primacy hierarchy since it comes from a single diagnostic, and it is a fundamental property of the turbulence. The nT crossphase angle α_{nT} is considered *second* in the hierarchy since it uses inputs from two different diagnostics and compares the properties of distinct fluctuating quantities. Lastly both ion and electron heat fluxes are considered *third* in the hierarchy because power-balance calculations take into account several experimental inputs as well as external models to arrive at the heat fluxes. In the case of TRANSP, density/temperature profiles require data from different diagnostics and a magnetic reconstruction which also uses magnetic probe experimental data. Profiles are thus at least second in the hierarchy. Additionally, TRANSP makes use of external models for ECRH absorption, Ohmic power deposition, and sawtooth behaviour which rely on second-order profiles and push the power balance calculation further away from being a fundamental measurement.

The measured cross-phase angle between the reflectometer's amplitude and the ECE signal was found to feature an opposite sign when compared with the synthetic density-temperature cross-phase estimates from both TGLF and GENE. However, the magnitudes of these cross-phase angles (see figures 8, 13, 18) seem to be in fair agreement between simulations and experiment. It has been suggested that there could be a phase difference between the reflectometer-amplitude signal and density fluctuations[86]. Without careful full-wave reflectometer modeling, which is beyond the scope of this publication, it is not clear whether the measured cross-phase angle between the reflectometer's amplitude and the ECE signal is truly an experimental observable for the nT crossphase. Nevertheless, in order to perform an impartial validation effort, the Ricci parameter framework will be applied here to all observables firstly ignoring the nT crossphase, secondly including the nT crossphase regardless of the sign disparity, and lastly using only the magnitude of the nT crossphase as an observable.

Central to any rigurous validation effort is the careful evaluation of the sources of potential uncertainty both in experimental and simulation fronts. Experimental uncertainty is generally well described since it is intrinsic to rigorous empirical measurement efforts. Uncertainties for the different observables have been discussed in detail in the experimental results IV A and power-balance V A sections above. On the other hand, simulation uncertainty is rarely addressed because of the difficulties quantifying it; however, it is just as important as experimental uncertainty to the quantification of experiment-simulation agreement. Beyond fundamental limitations inherent to any model, Ricci et al.[112] mention potential sources of simulation uncertainty: limited numerical accuracy, finite time series (statistical uncertainty), and imprecise input parameters. The latter includes inputs to the simulation such as uncertainty in profiles, gradients, and Z_{eff}, as well as imprecise details on the synthetic diagnostic interpretation such as the sampling beam radius.

B. TGLF validation study

This section proceeds to use the Ricci parameter framework to compare experimental results with those obtained from TGLF as presented in section V B. Four separate quantities will be used to validate TGLF: temperature fluctuation levels dT_e/T_e, nT crossphase angle α_{nT}, electron (Q_e), and ion (Q_i) heat fluxes.

Simulation uncertainty estimates of the output observables taken from TGLF simulations will be discussed now. Since TGLF calculates a unique solution to the turbulence properties and heat fluxes based on a given set of inputs, errors due to finite time series can be neglected. Errors due to limited numerical accuracy can affect the dT_e/T_e and α_{nT} synthetic diagnostic estimate. The default TGLF $k_\perp$ resolution is 1.02cm^{-1} (see symbols in Fig. 13(a)). In this study, the default $k_\perp$ grid was increased to 0.05cm^{-1} to define the diagnostic Gaussian function weight and linear interpolation was used to increase the $k_\perp$ resolution of the temperature fluctuation intensity function. If a step-wise interpolation was used instead, dT_e/T_e estimates could change up to 10%. The interpolation method was tested to have negligible effects in the α_{nT} observable.

Another important source of uncertainty, overlooked by previous validation studies of this kind, is the sensitivity of TGLF to imprecise input parameters. Taking a similar approach as taken above to estimate TRANSP heat flux uncertainty (see section V A), 30 independent simulations were performed where input gradients and Z_{eff} were varied to observe the sensitivity of TGLF outputs to input experimental uncertainty. Gradient and Z_{eff} input values were varied within the following 1σ experimental uncertainty (see section III): a/Ln_e by $\pm$ 20%, a/LT_e by 30%, a/LT_i by 10%, and Z_{eff} by 20%. In order to get an average output error estimate from random input error, each of these input uncertainties were varied randomly (Gaussian-distributed) in 30 separate simulations with a mean variation of zero and a standard-deviation of 1σ on each input. The results of this sensitivity scan yielded errors of $\Delta dT_e/T_e/dT_e/T_e = 38\%$, $\Delta\alpha_{nT}/\alpha_{nT} = 7\%$, $\Delta Q_e/Q_e = 33\%$, $\Delta Q_i/Q_i = 44\%$.

The synthetic diagnostic applied to TGLF outputs to extract dT_e/T_e and α_{nT} is also affected by uncertainty in the sampling beam radius (effective antenna pattern at measurement location). Since the position of the launching antenna, quasi-optical lenses, and vacuum window is known with an accuracy of 5 mm, 40 different ray-tracing simulations were performed varying these positions arbitrarily inside 2σ. Since the measurement locations were close to the beam waist, the standard deviation of changes to the beam radius was only 0.3 mm, while the average was observed to increase by 0.2 mm. Thus a conservative error bar of 0.5 mm was applied to the beam radius in the synthetic diagnostic. This beam radius error leads to an average error of 4% in dT_e/T_e and 3% in α_{nT}. This calculation ignores changes to the beam radius caused by inaccuracies or inhomogeneities in the refractive index of focusing elements, and it is left for future work to quantify this source of uncertainty. Another potential source of uncertainty in the estimation of the beam radius could be scattering of the beam due to turbulence in the SOL and the confined plasma near the separatrix, see Snicker et al.[113].

Observable	H_j	**Run ID** - Hydrogen	d_j	R_j	S_j
dT_e/T_e	1	Nominal-$\rho_{Tor}=0.65$	0.23	0.18	0.82
		Nominal-$\rho_{Tor}=0.75$	0.39	0.23	0.77
		VITALS-$\rho_{Tor}=0.65$	0.18	0.16	0.82
		VITALS-$\rho_{Tor}=0.75$	0.13	0.15	0.76
$\alpha_{n,T}$	0.5	Nominal-$\rho_{Tor}=0.65$	15.9	1.00	0.92
		Nominal-$\rho_{Tor}=0.75$	12.6	1.00	0.89
		VITALS-$\rho_{Tor}=0.65$	15.9	1.00	0.92
		VITALS-$\rho_{Tor}=0.75$	12.6	1.00	0.89
$\lvert\alpha_{n,T}\rvert$	0.5	Nominal-$\rho_{Tor}=0.65$	0.95	0.48	0.92
		Nominal-$\rho_{Tor}=0.75$	0.75	0.39	0.89
		VITALS-$\rho_{Tor}=0.65$	0.7	0.36	0.92
		VITALS-$\rho_{Tor}=0.75$	0.71	0.36	0.89
Q_e	0.33	Nominal-$\rho_{Tor}=0.65$	1.53	0.74	0.78
		Nominal-$\rho_{Tor}=0.75$	1.74	0.81	0.75
		VITALS-$\rho_{Tor}=0.65$	0.62	0.32	0.73
		VITALS-$\rho_{Tor}=0.75$	0.98	0.49	0.71
Q_i	0.33	Nominal-$\rho_{Tor}=0.65$	3.92	0.99	0.8
		Nominal-$\rho_{Tor}=0.75$	3.52	0.99	0.79
		VITALS-$\rho_{Tor}=0.65$	1.64	0.78	0.67
		VITALS-$\rho_{Tor}=0.75$	2.03	0.88	0.72

TABLE II. Validation table for nominal and VITALS TGLF simulations of hydrogen (36770) discharge.

Tables II, III, and IV show the Ricci validation tables for both isotopes at both locations studied here. These quantify the experiment-simulation agreement shown in figure 14. Both d_o and λ are equal to 1.0. These have been chosen to allow for a quick growth of R values towards 1.0 and observe a significant variation in χ_R between nominal and VITALS simulations; the fundamental results are not changed by this choice[112].

Three main global observations can be made from these tables. First, the agreement between experiment and simulation is generally better in deuterium than hydrogen. In this study,

Observable	H_j	**Run ID** - Deuterium	d_j	R_j	S_j
dT_e/T_e	1	Nominal-$\rho_{Tor}=0.65$	0.56	0.29	0.83
		Nominal-$\rho_{Tor}=0.75$	0.26	0.19	0.77
		VITALS-$\rho_{Tor}=0.65$	0.07	0.14	0.82
		VITALS-$\rho_{Tor}=0.75$	0.03	0.13	0.75
$\alpha_{n,T}$	0.5	Nominal-$\rho_{Tor}=0.65$	14.1	1.00	0.91
		Nominal-$\rho_{Tor}=0.75$	12.5	1.00	0.89
		VITALS-$\rho_{Tor}=0.65$	14.2	1.00	0.91
		VITALS-$\rho_{Tor}=0.75$	12.5	1.00	0.89
$\lvert\alpha_{n,T}\rvert$	0.5	Nominal-$\rho_{Tor}=0.65$	0.23	0.18	0.91
		Nominal-$\rho_{Tor}=0.75$	1.75	0.82	0.89
		VITALS-$\rho_{Tor}=0.65$	0.16	0.16	0.91
		VITALS-$\rho_{Tor}=0.75$	1.8	0.82	0.89
Q_e	0.33	Nominal-$\rho_{Tor}=0.65$	0.94	0.47	0.76
		Nominal-$\rho_{Tor}=0.75$	0.99	0.49	0.73
		VITALS-$\rho_{Tor}=0.65$	0.16	0.16	0.72
		VITALS-$\rho_{Tor}=0.75$	0.42	0.24	0.69
Q_i	0.33	Nominal-$\rho_{Tor}=0.65$	1.35	0.67	0.61
		Nominal-$\rho_{Tor}=0.75$	1.44	0.71	0.63
		VITALS-$\rho_{Tor}=0.65$	0.53	0.30	0.45
		VITALS-$\rho_{Tor}=0.75$	0.81	0.41	0.54

TABLE III. Validation table for nominal and VITALS TGLF simulations of deuterium (36974) discharge.

Isotope	**Run ID**	no α_{nT}		with α_{nT}		with $\lvert\alpha_{nT}\rvert$	
		χ_R	Q_R	χ_R	Q_R	χ_R	Q_R
Hyd	Nom-$\rho_T=0.65$	0.45	1.35	0.59	1.80	0.46	1.80
	Nom-$\rho_T=0.75$	0.50	1.29	0.63	1.74	0.47	1.74
	VIT-$\rho_T=0.65$	0.30	1.29	0.48	1.75	0.32	1.75
	VIT-$\rho_T=0.75$	0.36	1.24	0.53	1.69	0.36	1.69
Deu	Nom-$\rho_T=0.65$	0.39	1.28	0.55	1.73	0.33	1.73
	Nom-$\rho_T=0.75$	0.34	1.22	0.52	1.67	0.46	1.67
	VIT-$\rho_T=0.65$	0.16	1.20	0.39	1.66	0.16	1.66
	VIT-$\rho_T=0.75$	0.19	1.16	0.41	1.61	0.37	1.61

TABLE IV. Results of comparing experiments and TGLF simulations through Ricci's[112] validation metric χ_R and comparison quality Q_R.

this occurs because the Q_i observable is strongly ($\times 2-7$) overestimated in hydrogen and less so in deuterium (see d_j columns in tables II and III). Second, the VITALS algorithm helped in both radii and both isotopes to reduce the distance d_j of all observables and hence improved the final experiment-simulation agreement χ_R. The VITALS optimization results attempted to minimize errors on Q_e, Q_i, and dT_e/T_e simultaneously. This not only helped to better minimize discrepancies with experiments but also helped to better constraint the optimization problem. Lastly, while including the nT crossphase with its true experimental sign leads to a marked increase in χ_R, including the α_{nT} observable results in an increased comparison quality Q_R going from $Q_R \sim 1.2$ to $Q_R \sim 1.7$.

When looking at the comparison ignoring the nT crossphase, it is surprising to see that regardless of the strong distances in the Q_i observable, thanks to the large experimen-

tal (28%) and simulation (44%) uncertainty and low place in the hierarchy, the metric still assigns relative agreement ($\chi_R < 0.5$ in table IV) to all -even nominal- simulations. This is due to the relative success of the simulations in reproducing the electron heat flux and dT_e/T_e levels which both depend strongly on Q_e. Turbulence properties sit lower in the hierarchy and hence are assigned a larger weight. Such general agreement in the light of a strong Q_i overestimation encourages extending the number of observables to cover fluctuating quantities that affect ion heat transport, i.e. potential, density, and/or ion temperature fluctuations.

If the nT crossphase is included in the comparison, the sign disparity leads to very large distances d_j and a saturated $R_j = 1$ implying complete disagreement. Ricci parameters χ_R are found to increase to the point that all nominal simulations are found in general disagreement $\chi_R > 0.5$. However, in the case of deuterium VITALS simulations, the good agreement in all other observables still allows a marginal overall agreement between experiment and simulations. If only the nT crossphase magnitudes are used in the comparison the χ_Rs are only slightly increased from the no α_{nT} case and thus overall agreement between experiment and simulations is found but at a higher $Q_R \sim 1.7$. If only the electron and ion heat-fluxes were used in the validation, the quality would drop to $Q \sim 0.4$.

An important aspect of tables II and III is that the quantity S, which quantifies the precision of the comparison can reach values down to $S \sim 0.5-0.6$. This indicates that when adding the experimental and simulation uncertainties, certain observables have a combined uncertainty of up to $\sim 70\%$. This encourages a consideration of means to reduce experimental and simulation errors in an attempt to make observables more precise. Improving kinetic profile diagnostics and fitting techniques can directly reduce gradient scale-length uncertainty and lead to a reduction of all simulation uncertainties.

C. GENE validation study

This section proceeds to use the Ricci parameter framework to quantify the comparison between experimental data and the non-linear GENE simulations presented in section V C. Given the 2D nature and time-resolved results from GENE, five separate observables can be used in this case: temperature fluctuation levels dT_e/T_e, radial correlation lengths $L_{r,c}$, nT crossphase angles α_{nT}, electron (Q_e), and ion (Q_i) heat fluxes.

Simulation uncertainty estimates of the output observables taken from GENE simulations will be discussed now. Beyond errors due to model simplifications, modeling errors can be due to limited numerical accuracy, finite time series, and imprecise input parameters[112]. Finite time-series errors are addressed first. GENE solves the gyrokinetic equation over time and once a solution has converged, there is a natural small time variation in the estimates of the heat fluxes. Such numerical accuracy fluctuations lead to ion/electron heat-flux errors between 2 and 5%. Finite time-series errors affect all synthetic diagnostic observables. Averaging over different adjacent volumes has been performed to ameliorate this situation as described in section V C. Nonetheless, the standard deviation of the mean of synthetic estimates leads to errors of 6% in dT_e/T_e, and 3-11% in $L_{r,c}$ (depending on the goodness of fit), and 3-6% in α_{nT}. Numerical accuracy errors have also been explored. Linear interpolation is used between 2D grid fluctuation maps. For these simulations, the grid features resolutions of $\sim$0.5 mm in both horizontal and vertical dimensions. Increasing the resolution via polynomial or spline interpolation to better define the synthetic PSFs has negligible ($< 0.1\%$) effects in all observables.

Errors caused by imprecise input parameters are also very important. Uncertainties in input gradients and Z_{eff} affect all observables. Although relatively inexpensive flux-tube ion-scale simulations have been performed here, every simulation consumes between 256 and 768 node-hours in MARCONI-100 (CINECA) and CORI (NERSC), respectively. From a computing-resources perspective, it was not possible to perform many simulations in a Monte-Carlo-like fashion as done for TGLF above. Since linear simulations revealed dominant ITG turbulence in both isotopes, the ion temperature gradient a/LT_i was varied in 5 steps[24] (0.8, 0.9, 0.95, 1.0, and 1.2 $\cdot a/LT_i$) while keeping all other inputs constant, following the 1σ 20% a/LT_i GPR fit errors. This scan produced standard deviations of 13% in dT_e/T_e, 19% in $L_{r,c}$, 12% in α_{nT}, 15% in Q_e, and 45% in Q_i. The large change in Q_i due to a 1σ scan in a/LT_i leads to an equivalent GENE uncertainty which is twice as large as experimental power-balance Q_i uncertainty found at 23%. However, this mono-variate scan provides simply an indicative error bar; future work should attempt to address changes in other inputs as well. Finally, experimental uncertainty in the sampling beam radius ($\approx$0.5mm as explained in the section VI B) leads to an average error of 2% in dT_e/T_e, 2% in $L_{r,c}$, and 0.1% in α_{nT} GENE synthetic diagnostics.

Observable	H_j	**Run ID** - H	d_j	R_j	S_j
dT_e/T_e	1	Nom	1.44	0.71	0.91
		Best	0.26	0.19	0.90
$L_{r.c}$	1	Nom	0.92	0.46	0.87
		Best	1.51	0.73	0.88
$\alpha_{n,T}$	0.5	Nom	10.4	1.00	0.87
		Best	10.4	1.00	0.87
$\lvert\alpha_{n,T}\rvert$	0.5	Nom	0.50	0.27	0.87
		Best	0.39	0.23	0.87
Q_e	0.33	Nom	3.47	0.99	0.88
		Best	0.06	0.13	0.85
Q_i	0.33	Nom	5.92	1.0	0.87
		Best	0.55	0.29	0.74

TABLE V. Validation table for nominal and 'best-match' GENE simulations of hydrogen discharge 36770 at $\rho_{Tor} = 0.75$.

Based on these results, tables V and VI show the Ricci validation table containing distance R, precision S, and hierarchy H terms for each observable in both isotopes. These attempt to quantify the results of the comparison illustrated in

Observable	H_j	**Run ID** - D	d_j	R_j	S_j
dT_e/T_e	1	Nom	0.28	0.19	0.92
		Best	0.27	0.19	0.92
$L_{r,c}$	1	Nom	0.46	0.25	0.89
		Best	0.33	0.21	0.89
$\alpha_{n,T}$	0.5	Nom	10.1	1.00	0.87
		Best	10.7	1.00	0.88
$\lvert\alpha_{n,T}\rvert$	0.5	Nom	1.04	0.52	0.87
		Best	1.36	0.67	0.88
Q_e	0.33	Nom	0.68	0.35	0.85
		Best	0.25	0.18	0.84
Q_i	0.33	Nom	3.53	0.99	0.83
		Best	0.32	0.20	0.73

TABLE VI. Validation table for nominal and 'best-match' GENE simulations of deuterium discharge 36974 at $\rho_{Tor} = 0.75$.

Isotope	**Run ID**	no α_{nT}		with α_{nT}		with $\lvert\alpha_{nT}\rvert$	
		χ_R	Q_R	χ_R	Q_R	χ_R	Q_R
Hyd	Nom	0.69	2.36	0.74	2.8	0.62	2.8
	Best	0.39	2.31	0.49	2.7	0.37	2.7
Deu	Nom	0.33	2.37	0.43	2.8	0.36	2.8
	Best	0.19	2.33	0.32	2.8	0.27	2.8

TABLE VII. Results of comparing experiments and GENE simulations through Ricci's[112] validation metric χ and comparison quality Q_R at $\rho_{Tor} = 0.75$.

figure 19. The final Ricci validation metric χ_R and validation quality Q_R is shown in table VII. Both d_o and λ are equal to 1.0 to be consistent with section VI B. These tables can be directly compared against their TGLF analogs, tables II, III, and IV.

The general observations are similar to those found in the TGLF-SAT2 validation exercise. Firstly, the agreement is better in deuterium than in hydrogen. This also occurs here because the ion heat flux Q_i observable is seen more strongly overestimated in hydrogen than in deuterium. Secondly, the empirical 'best' heat-flux-match simulations significantly bring discrepancies down. The ion heat flux was brought within $2-\sigma$ error bars with experiments in both isotopes and hence $d_j \sim 0.5$ and $R_j < 0.3$s are found lower in tables V and VI than II and III. Lastly, taking the α_{nT} observable into account with its opposing sign leads to worsened experiment-simulation agreement (higher χ_R) in both isotopes than when it is ignored. However, the comparison quality is seen to increase from $Q_R \sim 2.3$ to $Q_R \sim 2.8$.

Table VII shows that even the best-match hydrogen simulations can find only marginal agreement with experiments when considering the opposing experimental α_{nT} sign ($\chi_R \sim 0.5$). This is because of the strong disagreement in α_{nT} as well as mild disagreement in Q_i and $L_{r,c}$. Deuterium simulations do a lot better to the point that even nominal simulations in the light of the α_{nT} disparity still find general agreement. This is because of the excellent agreement on all the rest of observables dT_e/T_e, $L_{r,c}$, and Q_e which are all related to electron heat transport. Such general agreement in the light of a $Q_i \times 2-3$ overestimation encourages extending the number of observables to cover fluctuating quantities that affect ion heat transport.

Tables V and VI show that the the sign disparity in the α_{nT} observable - as seen already with TGLF-SAT2 - leads to large $d_j \sim 10$ and saturated $R_j = 1$. χ_R validation metrics are seen to increase when compared with validations ignoring the observable. If only the $\lvert\alpha_{nT}\rvert$ magnitudes are used in the comparison, however, the level of agreement between experiments and simulations remains relatively close to those ignoring α_{nT} and even goes down (improving agreement) for hydrogen best-match simulations. While the sign discrepancy is an important open issue, the fact that the magnitude of α_{nT} moved in the right direction when changing isotope masses demonstrates that the observable holds promise.

The validation quality Q_R reported in table VII is about $Q \sim 2.3$ without α_{nT}, and it reaches $Q \sim 2.8$ including α_{nT}. If only heat-fluxes had been used in the experiment-modelling comparison, the quality would have droped to $Q \sim 0.5$. The comparison qualities are seen to be larger than in the TGLF validation table IV, because of the presence of an additional observable in the GENE simulations: $L_{r,c}$. Beyond the additional observable, it must be stressed that the unique velocity space coordinates of GENE allow to discern parallel and perpendicular dT_e/T_e contributions[98] which are central to compare with experiments and allowed TGLF's total dT_e/T_e estimate to be quantitatively compared with experiments in section VI B above.

Errors due to model simplifications are difficult to evaluate quantitatively and are not included in the validation study above. However, the simulations performed elucidated potential avenues for future model improvements. Much better agreement between experiment and simulation was found when the measured Z_{eff} was modeled via a third-species. In this case Boron was used to model impurities, and the density gradients were taken from electron density profiles. It is not clear whether Boron is indeed the main/dominant impurity or could be replaced by one or more other species (informed perhaps by spectroscopic measurements of main impurities). It is also not clear whether the impurity species density gradient is indeed identical to that of the electron density gradient.

Additionally, it is important to note that potentially relevant turbulence drives have not been scanned in search for the 'best-match' simulation. Future work could focus on scanning MHD equilibrium reconstruction uncertainty which can lead to changes to the safety factor (q) as well as q-shear. These could play an important role in energy transport. Also, the T_e/T_i ratio has not been scanned. Finally, heat-flux overestimations could also be due to missing finite-size effects which would reduce transport and would require global simulations. However, the rho-star $\rho^* = 1/436$ in deuterium and $\rho^* = 1/643$ in hydrogen which are both $\ll 1$ (see Appendix B). The latter provides confidence in the flux-tube approximation.

VII. SUMMARY

This work has addressed the turbulence and energy transport properties of a pair of L-mode plasmas in the AUG tokamak featuring the same density and external input power but different ion masses: deuterium and hydrogen. Ion-scale ($k_\perp \rho_s < 0.2$) fluctuation measurements and interpretative power balance revealed important experimental features:

(1) Electron temperature fluctuations were larger in deuterium than hydrogen, dT_e/T_e(D)> dT_e/T_e(H). Measurements inside $\rho_{Tor} = 0.75-0.8$ showed that the ratio of fluctuation levels is in agreement with an ion-Larmor radius ratio, consistent with mixing-length arguments.

(2) Radial correlation lengths were larger in deuterium than in hydrogen, $L_{r,c}$(D)> $L_{r,c}$(H). Measurements inside $\rho_{Tor} = 0.75-0.8$ show a ion-Larmor radius scaling where $L_{r,c} \sim 5-6\rho_i$, independent of ion-mass.

(3) The cross-phase angle between a reflectometer amplitude and a ECE signal was found larger in amplitude and more out-of-phase in hydrogen ($\alpha_{RefA-ECE}$(H)= $150 \pm 20^\circ$) than in deuterium ($\alpha_{RefA-ECE}$(D)= $100 \pm 16^\circ$) at $\rho_{Tor} = 0.75$. The sign of this cross-phase angle was found positive in contrast with previous results in L-mode plasmas[23,24,78]. Nonetheless, the larger cross-phase angle magnitude in hydrogen over deuterium is consistent with an increased ITG drive in hydrogen due to the larger ion-temperature gradient observed in the hydrogen discharge.

(4) Thanks in great part to the electron-ion heat exchange term ($p_{e,i}$), the ion heat flux was larger in hydrogen than in deuterium Q_i(H)> Q_i(D) outside of error bars. Electron heat fluxes were found larger in deuterium but well inside error bars with Q_e(D)$\gtrapprox$ Q_e(H).

A validation study was then conducted with the quasi-linear gyro-Landau fluid TGLF-SAT2 and non-linear gyrokinetic GENE codes. The central question was whether these models could reproduce the changes of turbulence and energy transport properties with isotope mass observed in experiments, within 1σ experimental error. The validation exercise considered experimental as well as simulation uncertainties and attempts to quantify agreement using the Ricci validation methodology[112].

Quasi-linear gyrofluid TGLF-SAT2 simulations were performed locally at $\rho_{Tor} = 0.65$ and 0.75 in both isotopes. New synthetic diagnostics were introduced where a Gaussian function representing the diagnostic antenna pattern in wavenumber space[72] is used to rigurously extract synthetic dT_e/T_e levels and α_{nT}. TGLF-SAT2 was successful in recovering experimental trends (1) and (4) above. The density-temperature cross-phase angle was found to be negative in all simulations; however, the cross-phase angle magnitudes were found to be in rough agreement. TGLF-SAT2 failed nonetheless to recover experimental trend (3) showing an almost constant α_{nT} with changing isotope mass. Radial correlation lengths $L_{r,c}$ (2) could not be extracted from TGLF-SAT2. Nominal input profiles led to a strong over-prediction of ion-heat fluxes in both radii, especially in hydrogen where the overprediction reached up to a $\times 7$ factor. In spite of a careful iteration of input profile gradients, $v_{E\times B}$ shearing rates, and Z_{eff} within 1σ errors done using the VITALS framework[100], the ion heat flux could not be matched. However, the electron heat flux, dT_e/T_e, and $|\alpha_{nT}|$ could be brought within 2σ.

When taking all observables into account, including the markedly different sign in α_{nT}, nominal input gradient simulations in both isotopes are found in general disagreement with experiment: $\chi_R \geq 0.57$[112]. VITALS simulations bring the discrepancies down significantly with deuterium finding general agreement $\chi_R \approx 0.4$ but hydrogen still showing marginal agreement $\chi_R \approx 0.5$. If only the magnitudes of the $|\alpha_{nT}|$ observable are taken into account in the validation, the agreement improves significantly with $\chi_R \approx 0.3$ in hydrogen and $\chi_R \approx 0.25$ in deuterium. The quality of the validation featuring 4 separate observables reached $Q_R \approx 1.7$. If only heat fluxes had been used in the validation, the quality of the comparison would have been only $Q_R \approx 0.4$. The consistent Q_i overestimation encourages the addition of further observables to the validation, specially those capable of constraining quantities relevant to ion heat transport, i.e. potential, density, and/or ion temperature fluctuations.

Nonlinear, fluxtube δf, gyrokinetic simulations were performed at $\rho_{Tor} = 0.75$ with the GENE code. These were able to successfully recover all experimental trends (1) through (4) once heat flux matched simulations were obtained by varying input gradients and Z_{eff}. A third-species was introduced in the simulations to model the measured Z_{eff}. Good general agreement within 2σ in all observables and both isotopes was reached - in contrast to TGLF-SAT2. The level of agreement reported in GENE simulations was possible thanks to several improvements in synthetic diagnostics. Firstly, modeling the diagnostic antenna pattern through TORBEAM allowed the heat-flux matched synthetic-GENE and CECE dT_e/T_e estimates to agree within 1σ error bars. Secondly, the effect of changing the amplitude of the $E \times B$ rotation in the synthetic CECE spectra was investigated for the first time. It was shown conclusively that the location of peak of the CECE dT_e/T_e spectrum depends on the amplitude of the $E \times B$ rotation, in agreement with experimental trends. Using E_r estimates from DBS as input to GENE simulations led to a closer agreement with the shape of the experimental CECE spectra. In addition, a new formula to compute radial correlation lengths from multi-channel uncalibrated CECE radiometers is proposed which uses normalized cross-correlation coefficients in agreement with standard texts[62,114] and other fluctuation diagnostics[28]. Synthetic radial correlation lengths are found in agreement within 1σ error bars with experiments in deuterium and within 2σ in hydrogen. Lastly, the n-T cross-phase angle was found negative in GENE in agreement with TGLF-SAT2 but in contrast with experiments. Interestingly, however, the magnitude of the synthetic cross-phase angle was found to agree within 2σ error bars and follow the experimental trend with larger $|\alpha_{nT}|$ in hydrogen over deuterium. A more out-of-phase α_{nT} is consistent with linear simulations showing a

stronger ITG drive in the hydrogen discharge.

Ricci parameters in the case of GENE nominal input simulations are found to be $\chi_R \approx 0.7$ and $\chi_R \approx 0.4$ for hydrogen and deuterium discharges, respectively. The strong discrepancy in hydrogen is driven by an overestimate in $Q_i \times 4$ and the sign discrepancy in α_{nT}. In the case of deuterium, in spite of a $Q_i \times 3$ overestimation and the α_{nT} sign discrepancy, the nominal input simulations achieve general agreement with experiment. This is possible because Q_i features large error bars and a modest position in the primacy hierarchy while good agreement in dT_e/T_e, $L_{r,c}$, and Q_e drives the nominal-input simulation towards agreement. Scanning input gradients and Z_{eff} inside error bars brings hydrogen simulations towards marginal agreement $\chi_R \approx 0.5$ and deuterium simulations towards better agreement $\chi_R \approx 0.3$. If only the magnitudes of $|\alpha_{nT}|$ are used in the validation, then both isotopes are found in general agreement with experiment with $\chi_R(H) \approx 0.37$ and $\chi_R(D) \approx 0.27$. The quality of GENE validation is $Q_R \approx 2.8$ achieved thanks to five different observables compared to $Q_R \approx 0.5$ using only heat-fluxes. Similarly to the findings with TGLF-SAT2, the ion heat flux was the hardest quantity to match in both isotopes, specially hydrogen. Due to the large amount of computing resources required to run GENE, a full sensitivity study to input uncertainties was not possible and hence simulation error bars feature a scan of ion-temperature gradient only and are thus approximate.

Even though efforts were made to produce the highest-quality average profile fits, nominal input gradient simulations featured an average $\chi_R \geq 0.5$ in both gyrofluid and gyrokinetic simulations. This highlights the importance of considering profile and gradient uncertainties when predicting the turbulent transport of future tokamak devices. Efforts to reduce the input profile uncertainties would be highly welcome to reduce simulation uncertainties in all observables as well as to increase the quality - and hence confidence - of validation efforts.

The standing sign discrepancy between cross-phase angles $\alpha_{RefA-ECE}$ from experiments and α_{nT} from both TGLF-SAT2 and GENE simulations encourages further research on this observable. This discrepancy is particularly strange given the good agreement in other turbulence observables. The magnitude of experimental $|\alpha_{RefA-ECE}|$ is found to follow experimental changes to turbulence drives and roughly agrees with $|\alpha_{nT}|$ from simulations; therefore, this observable shows undeniable promise. Future work could focus in full-wave 2D simulations of fluctuation reflectometry[115] which can help in clarifying under which conditions the reflectometer's amplitude signal is and is not a sound kernel for density fluctuations[116]. Using alternative measurements with a clearer interpretation as density fluctuations may also offer a way forward. For example, pulse group-delays from short-pulse reflectometry[117] could be used since these signals perform time-domain filtering of back-scattered signals away from the cut-off, and it has been recently used to extract both density fluctuation amplitudes and radial correlation lengths[118]. Additionally, other established density-fluctuation diagnostics such as beam-emission spectroscopy[67] could be used, albeit with the experimental difficulty regarding alignment with CECE observational volumes.

Global energy confinement time (obtained via TRANSP power-balance[43]) is found larger in deuterium than hydrogen τ_E(D)= 85ms (36974) > τ_E(H)= 72ms (36770). However, local electron temperature fluctuations in the outer-core showed a gyro-Bohm scaling which is consistent with a larger electron heat flux in deuterium over hydrogen $Q_e(\text{D}) \gtrapprox Q_e(\text{H})$. However, τ_E also depends on the ion heat transport where Q_i(H)> Q_i(D). Linear solvers indicate that, at long wavelengths, energy transport in the deuterium discharge is dominated by a mixed ITG-TEM turbulence while in hydrogen transport is exclusively and more strongly driven by ITG turbulence. The latter is confirmed by a larger ion temperature gradient a/LT_i and nT cross-phase angle observed in hydrogen. The improved energy confinement in deuterium can be hypothesized to be due to the fact that the external electron heating is most efficiently coupled to the ions in the hydrogen discharge and that the stronger ITG drive in hydrogen releases this energy more efficiently and leads to a worsened confinement. This hypothesis was first proposed in Schneider et al.[25], and this study finds it still valid in L-mode plasmas at half the line-integrated density. Future work could attempt a similar multi-observable study including more fluctuation observables as well as more plasma regions such as the plasma edge[40,41].

VIII. ACKNOWLEDGEMENTS

Omar Maj and Emmanuele Poli are gratefully acknowledged for useful advice and discussions regarding the propagation of ECE waves in tokamak plasmas and for their assistance with the TORBEAM and WKB codes. Phillip Schneider is also gratefully acknowledged for insightful discussions regarding isotope effects in discharge planning and analysis. Furthermore, Gary Staebler and Clemente Angioni are acknowledged for their assistance with understanding and preparing TGLF input files in the AUG environment. Lastly, Rachael McDermott's help with CXRS data analysis is thankfully acknowledged.

This work is supported by the US Department of Energy under grants DE-SC0014264, DE-SC0006419, and DE-SC0017381. This work has been carried out within the framework of the EUROfusion Consortium, funded by the European Union via the Euratom Research and Training Programme (Grant Agreement No 101052200 — EUROfusion). Views and opinions expressed are however those of the author(s) only and do not necessarily reflect those of the European Union or the European Commission. Neither the European Union nor the European Commission can be held responsible for them. This research used resources of the National Energy Research Scientific Computing Center (NERSC), a U.S. Department of Energy Office of Science User Facility located at Lawrence Berkeley National Laboratory, operated under Contract No. DE-AC02-05CH11231 using NERSC award ERCAP0017049 (2021) and ERCAP0020063 (2022) and HPC resources from CINECA Marconi-Fusion.

Appendix A: Correlation length estimate

This section describes the derivation of equation 3. An ECE radiometer signal observing an optically thick ECE emission layer contains three main contributions[16]: a DC portion directly proportional to the plasma temperature (T_e), a temperature fluctuation component (dT_e), and a thermal (black-body) noise component ($\widetilde{N}_x$).

$$x(t) \approx c_x(T_e + dT_e(t) + T_e\widetilde{N}_x(t)), \tag{A1}$$

where c_x is a calibration coefficient. The $\widetilde{N}_x$ term dominates the time-dependant portion of the ECE radiometer signal[61 60] and is the reason why ensemble averaging over steady plasma conditions is required to measure temperature fluctuations with correlation-ECE. This equation assumes that the radiometer is operating in its nominal, linear-response, input power regime for both RF and IF amplifier stages. In order to estimate the radial correlation length of temperature fluctuations, analytical efforts must isolate the temperature fluctuation component from the ECE signal and use standard statistical tools[62] to access the spatial self-coherence over a number of spatially separated channels. Standard texts[62,114] and established plasma diagnostics[28] make use of the normalized cross-correlation coefficient at zero time-delay:

$$\begin{aligned}\rho_{xy}(\tau=0) &= \frac{\langle x(t)y^*(t)\rangle}{\sqrt{\langle|x(t)|^2\rangle\langle|y(t)|^2\rangle}},\\ &= \frac{R_{xy}(\tau=0)}{\sqrt{R_{xx}(\tau=0)R_{yy}(\tau=0)}},\\ &= \frac{\int G_{xy}(f)df}{\sqrt{\int G_{xx}(f)df\int G_{yy}(f)df}},\end{aligned}$$

where $R_{xy}(\tau=0)$ is the cross correlation at zero time delay, and G_{xy} is the cross-power spectral density. The following relationship[62] between the mean square (Ψ_x^2), R_{xy}, and G_{xy} has been used: $\Psi_x^2 = R_{xx}(\tau=0) = \int_{-\infty}^{\infty} G_{xx}(f)df$. Using auto/cross power spectral densities is preferred since it allows the computation of ρ_{xy} to take place in the frequency domain where the drift-wave turbulence and electronics noise features can be most easily separated[119].

Since one is interested in the cross-correlation coefficient of temperature fluctuations, the auto/cross power spectra should make explicit use of the portion of the CECE signal $dT_e(t)$. Allowing $dT_e(f)$ to be the Fourier transform of the latter, the cross-correlation coefficient can be expressed as:

$$\rho_{xy}(\tau=0) = \frac{\int\langle dT_{e,x}(f)^*dT_{e,y}(f)\rangle df}{\sqrt{\int\langle|dT_{e,x}(f)|^2\rangle df\cdot\int\langle|dT_{e,y}(f)|^2\rangle df}}.$$

Following the nomenclature in the Appendix of Creely et al.[16], let the cross ($G_{xy} = \langle X(f)^*Y(f)\rangle$) and auto ($G_{xx} = \langle X(f)^*X(f)\rangle$) spectral power density from two ECE radiometer channels, which can be far apart from each other and thus do not share a common DC electron temperature (T_e) be given as:

$$\begin{aligned}G_{xy}(f) &= c_xc_y\left(\langle dT_{e,x}(f)^*dT_{e,y}(f)\rangle + T_{e,x}T_{e,y}\widetilde{N}_{x,y}^2(f)\right),\\ G_{xx}(f) &= c_x^2\left(\langle|dT_{e,xx}(f)|^2\rangle + T_{e,x}^2\widetilde{N}_x^2(f)\right),\end{aligned} \tag{A2}$$

where equation A1 defines the signal x(t) or y(t), $dT_{e,xx}(f) = \langle dT_{e,x}(f)^*dT_{e,x}(f)\rangle$, and $\widetilde{N}_x(f)$ is the fourier transform of noise term $\widetilde{N}_x(t)$ in equation A1, and $\widetilde{N}_{x,y}^2(f) = \langle\widetilde{N}_x(f)^*\widetilde{N}_y(f)\rangle$. Assuming, in order to keep equations tractable, in the case of the auto-power spectral density that the signal is dominated by the black body noise contributions[119] $T_{e,x}^2\widetilde{N}_x^2(f) \gg dT_{e,xx}^2(f)$, thus, let $G_{xx} \approx c_x^2(T_{e,x}^2\widetilde{N}_x^2)$. Using the latter to solve for the calibration coefficients c_x and c_y in equation A2 and dropping the frequency dependencies to simplify notation, the relevant fluctuating quantity required to calculate $\rho_{xy}(\tau=0)$ is solved as:

$$\begin{aligned}\langle dT_{e,x}^*dT_{e,y}\rangle &= \frac{G_{xy}-G_{noise}}{c_xc_y},\\ &= \frac{G_{xy}-G_{noise}}{\sqrt{\frac{G_{xx}}{T_{e,x}^2\widetilde{N}_x^2}\frac{G_{yy}}{T_{e,y}^2\widetilde{N}_y^2}}},\\ &= (\gamma_{xy}(f)-\gamma_{bg})T_{e,x}T_{e,y}\widetilde{N}_x\widetilde{N}_y,\end{aligned}$$

where $G_{noise} = c_xc_yT_{e,x}T_{e,y}\widetilde{N}_{x,y}^2$ is the part of the cross-power spectrum due to finite filter overlap. $\gamma_{xy/bg} = G_{xy/noise}/\sqrt{G_{xx}G_{yy}}$ stands for the complex cross-coherence. The normalized cross-correlation coefficient then becomes:

$$\begin{aligned}\rho_{xy}(\tau=0) &= \frac{\int(\gamma_{xy}(f)-\gamma_{bg})T_{e,x}T_{e,y}N_xN_ydf}{\sqrt{\int\langle|dT_{e,x}(f)|^2\rangle df\int\langle|dT_{e,y}(f)|^2\rangle df}}\\ &= \frac{\int(\gamma_{xy}(f)-\gamma_{bg})N_xN_ydf}{\sqrt{|dT_{e,x}/T_{e,x}|^2|dT_{e,y}/T_{e,y}|^2}}\\ &= \frac{2\int(\gamma_{xy}(f)-\gamma_{bg})df}{B'_{IF}\sqrt{|dT_{e,x}/T_{e,x}|^2|dT_{e,y}/T_{e,y}|^2}}\end{aligned} \tag{A3}$$

where fourier transform of noise contributions $\widetilde{N}_x$ and $\widetilde{N}_y$ are assumed to follow a radiometer broad-band thermal (black-body) noise formula $\widetilde{N}_{x/y}^2 = 2/B_{IF,x/y}$[16] and thus $B'_{IF} = \sqrt{B_{IF,x}B_{IF_y}}$. In order to stay consistent with the assumption $T_e^2\widetilde{N}_x^2 \gg dT_{e,xx}^2$, the formula for the fluctuation level between two neighbour channels ($dT_{e,(x,x')}/T_{e,(x,x')}$) becomes the more traditional version as derived in Sung et al.[119]:

$$\begin{aligned}\left|\frac{dT_{e,(x,x')}}{T_{e,(x,x')}}\right|^2, &= \frac{1}{T_{e,(x,x')}^2}\int\langle|dT_{e,(x,x')}(f)|^2\rangle df,\\ &= \frac{2}{B_{IF'}}\int|\gamma_{xx'}(f)-\gamma_{bg}|df.\end{aligned} \tag{A4}$$

Due to the fact that equation A3 requires the fluctuation at the location of a single channel and not in-between two channels, the fluctuation levels with channels in front and behind the specific channel are averaged to estimate the fluctuation at a given channel. It is this average fluctuation level that enters in the denominator of equation A3 using equation A4. This averaging is ilustrated figure 20.

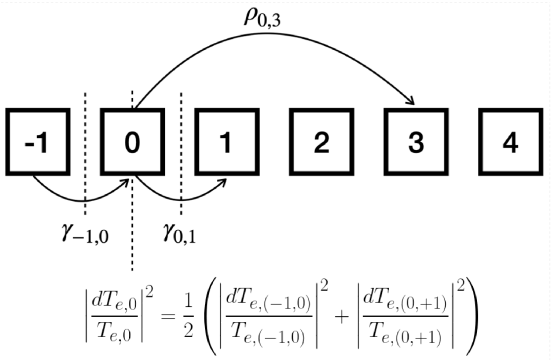

FIG. 20. Ilustration of averaging between two estimates of temperature fluctuation levels to arrive at estimate of fluctuation level at a single channel.

Equation A3 thus allows for the computation of the *normalized* cross-correlation coefficient of an uncalibrated radiometer in the frequency domain taking into account exclusively the temperature fluctuation component of the CECE signal.

Appendix B: GENE simulation input parameters

Parameter	Deuterium	Hydrogen
Shot number	36974	36770
ρ_{Tor}	0.75	0.75
r/a	0.765	0.765
T_i[eV]	397	400
T_e[eV]	648	593
T_i/T_e	0.613	0.674
$n_e[\mathrm{m}^{-3}]\times 10^{19}$	1.78	1.74
Z_{eff}	1.79	1.45
B_o (B at axis) [T]	-2.48	-2.48
q	-2.26	-2.27
shear $s = \rho_T/qdq/d\rho_T$	2.025	2.029
$\alpha = \sqrt{\phi_{sep}/(\pi B_o)}$[m]	0.645	0.643
α/LT_i	2.443	3.315
α/LT_e	4.265	3.622
α/Ln_e	0.707	0.579
c_s [km/s]	175	238
ρ_s[mm]	1.48	1.01
$\rho^* = \rho_s/\alpha$	1/436	1/643
$\beta_{ref} = 8\pi n_e T_e/B^2_{ref}$	$7.57{\cdot}10^{-4}$	$6.77{\cdot}10^{-4}$
$\gamma_{E\times B} = -\frac{\alpha}{c_s}\frac{\rho}{q}\frac{d\Omega_{Tor}}{d\rho}$ [1/s]	$2.6{\cdot}10^{-2}$	$9.97{\cdot}10^{-3}$
$\nu_c = \pi \log_e e^4 n_e \alpha/(\sqrt{2}^3 T_e^2)$	$9.58{\cdot}10^{-4}$	$1.10{\cdot}10^{-3}$

TABLE VIII. Nominal GENE non-linear simulation input parameters. See Goerler [98] for further details on parameter definition.

REFERENCES

[1] M. Bessenrodt-Weberpals, F. Wagner, O. Gehre, L. Giannone, J. Hofmann, A. Kallenbach, K. McCormick, V. Mertens, H. Murmann, F. Ryter, B. Scott, G. Siller, F. Soldner, A. Stabler, K.-H. Steuer, U. Stroth, N. Tsois, H. Verbeek, and H. Zoohm, Nuclear Fusion **33**, 1205 (1993).

[2] F. W. Perkins, C. W. Barnes, D. W. Johnson, S. D. Scott, M. C. Zarnstorff, M. G. Bell, R. E. Bell, C. E. Bush, B. Grek, K. W. Hill, D. K. Mansfield, H. Park, A. T. Ramsey, J. Schivell, B. C. Stratton, and E. Synakowski, Physics of Fluids B: Plasma Physics **5**, 477 (1993).

[3] H. Weisen, C. F. Maggi, M. Oberparleiter, F. J. Casson, Y. Camenen, S. Menmuir, L. Horvath, F. Auriemma, T. W. Bache, N. Bonanomi, A. Chankin, E. Delabie, L. Frassinetti, J. Garcia, C. Giroud, D. King, R. Lorenzini, M. Marin, P. A. Schneider, P. Siren, J. Varje, E. Viezzer, and JET contributors, Journal of Plasma Physics **86**, 905860501 (2020).

[4] M. O. Hagler and M. Kristiansen, *An Introduction to Controlled Thermonuclear Fusion*, 1st ed. (Lexington Books, Lexington, MA, Marc, 1979).

[5] G. McKee, C. Petty, R. Waltz, C. Fenzi, R. Fonck, J. Kinsey, T. Luce, K. Burrell, D. Baker, E. Doyle, X. Garbet, R. Moyer, C. Rettig, T. Rhodes, D. Ross, G. Staebler, R. Sydora, and M. Wade, Nuclear Fusion **41**, 1235 (2001).

[6] P. Hennequin, R. Sabot, C. Honoré, G. T. Hoang, X. Garbet, A. Truc, C. Fenzi, and A. Quéméneur, Plasma Physics and Controlled Fusion **46**, B121 (2004).

[7] E. Holzhauer, G. Dodel, and ASDEX Team, Review of Scientific Instruments **61**, 2817 (1990).

[8] A. J. Wootton, M. E. Austin, R. D. Bengtson, J. A. Boedo, R. V. Bravenec, D. L. Brower, J. Y. Chen, G. Cima, P. H. Diamond, R. D. Durst, P. H. Edmonds, S. P. Fan, M. S. Foster, J. C. Forster, R. Gandy, K. W. Gentle, R. L. Hickok, Y. X. Hey, S. K. Kim, Y. J. Kim, H. Lin, N. C. Luhmann, S. C. McCool, W. H. Miner, A. Ouroua, D. M. Patterson, W. A. Peebles, P. E. Phillips, B. Richards, C. P. Ritz, T. L. Rhodes, D. W. Ross, W. L. Rowan, P. M. Schoch, D. Sing, E. J. Synakowski, P. W. Terry, K. W. Wenzel, J. C. Wiley, X. Z. Yang, X. H. Yu, Z. Zhang, and S. B. Zheng, Plasma Physics and Controlled Fusion **30**, 1479 (1988).

[9] G. Cima, R. V. Bravenec, A. J. Wootton, T. D. Rempel, R. F. Gandy, C. Watts, and M. Kwon, Physics of Plasmas **2**, 720 (1995).

[10] S. Sattler and H. J. Hartfuss, Physical Review Letters **72**, 653 (1994).

[11] C. Watts, R. F. Gandy, T. D. Rempel, and G. Cima, Review of Scientific Instruments **66**, 451 (1995).

[12] B. H. Deng, C. W. Domier, N. C. Luhmann, D. L. Brower, A. J. H. Donné, T. Oyevaar, and M. J. van de Pol, Physics of Plasmas **8**, 2163 (2001).

[13] R. P. Hsia, B. H. Deng, W. R. Geck, C. Liang, C. W. Domier, N. C. Luhmann, Jr., D. L. Brower, and G. Cima, Review of Scientific Instruments **68**, 488 (1997).

[14] U. Stroth, D. Aguiam, E. Alessi, C. Angioni, N. Arden, R. A. Parra, V. Artigues, O. Asunta, M. Balden, V. Bandaru, A. Banon-Navarro, K. Behler, A. Bergmann, M. Bergmann, J. Bernardo, M. Bernert, A. Biancalani, R. Bielajew, R. Bilato, G. Birkenmeier, T. Blanken, V. Bobkov, A. Bock, T. Body, T. Bolzonella, N. Bonanomi, A. Bortolon, B. Böswirth, C. Bottereau, A. Bottino, H. van den Brand, M. Brenzke, S. Brezinsek, D. Brida, F. Brochard, C. Bruhn, J. Buchanan, A. Buhler, A. Burckhart, Y. Camenen, B. Cannas, P. C. Megias, D. Carlton, M. Carr, P. Carvalho, C. Castaldo, M. Cavedon, C. Cazzaniga, C. Challis, A. Chankin, C. Cianfarani, F. Clairet, S. Coda, R. Coelho, J. Coenen, L. Colas, G. Conway, S. Costea, D. Coster, T. Cote, A. Creely, G. Croci, D. C. Zabala, G. Cseh, A. Czarnecka, I. Cziegler, O. D'Arcangelo, A. D. Molin, P. David, C. Day, M. de Baar, P. de Marné, R. Delogu, S. Denk, P. Denner, A. Di Siena, J. D. Palacios Durán, D. Dunai, A. Drenik, M. Dreval, R. Drube, M. Dunne, B. Duval, R. Dux, T. Eich, S. Elgeti, A. Encheva, K. Engelhardt, B. Erdös, I. Erofeev, B. Esposito, E. Fable, M. Faitsch, U. Fantz, M. Farnik, H. Faugel, F. Felici, O. Ficker, S. Fietz, A. Figueredo, R. Fischer, O. Ford, L. Frassinetti, M. Fröschle, G. Fuchert, J. Fuchs,

H. Fünfgelder, S. Futatani, K. Galazka, J. Galdon-Quiroga, D. G. Escolà, A. Gallo, Y. Gao, S. Garavaglia, M. G. Muñoz, B. Geiger, L. Giannone, S. Gibson, L. Gil, E. Giovannozzi, S. Glöggler, M. Gobbin, J. G. Martin, T. Goodman, G. Gorini, T. Görler, D. Gradic, G. Granucci, A. Gräter, H. Greuner, M. Griener, M. Groth, A. Gude, L. Guimarais, S. Günter, G. Haas, A. Hakola, C. Ham, T. Happel, N. den Harder, G. Harrer, J. Harrison, V. Hauer, T. Hayward-Schneider, B. Heinemann, T. Hellsten, S. Henderson, P. Hennequin, A. Herrmann, E. Heyn, F. Hitzler, J. Hobirk, K. Höfler, J. Holm, M. Hölzl, C. Hopf, L. Horvath, T. Höschen, A. Houben, A. Hubbard, A. Huber, K. Hunger, V. Igochine, M. Iliasova, T. Ilkei, K. I. Björk, C. Ionita-Schrittwieser, I. Ivanova-Stanik, W. Jacob, N. Jaksic, F. Janky, A. Jansen van Vuuren, A. Jardin, F. Jaulmes, F. Jenko, T. Jensen, E. Joffrin, A. Kallenbach, S. Kálvin, M. Kantor, A. Kappatou, O. Kardaun, J. Karhunen, C.-P. Käsemann, S. Kasilov, A. Kendl, W. Kernbichler, E. Khilkevitch, A. Kirk, S. K. Hansen, V. Klevarova, G. Kocsis, M. Koleva, M. Komm, M. Kong, A. Krämer-Flecken, K. Krieger, A. Krivska, O. Kudlacek, T. Kurki-Suonio, B. Kurzan, B. Labit, K. Lackner, F. Laggner, A. Lahtinen, P. Lang, P. Lauber, N. Leuthold, L. Li, J. Likonen, O. Linder, B. Lipschultz, Y. Liu, A. Lohs, Z. Lu, T. Luda di Cortemiglia, N. Luhmann, T. Lunt, A. Lyssoivan, T. Maceina, J. Madsen, A. Magnanimo, H. Maier, J. Mailloux, R. Maingi, O. Maj, E. Maljaars, P. Manas, A. Mancini, A. Manhard, P. Mantica, M. Mantsinen, P. Manz, M. Maraschek, C. Marchetto, L. Marrelli, P. Martin, A. Martitsch, F. Matos, M. Mayer, M.-L. Mayoral, D. Mazon, P. McCarthy, R. McDermott, R. Merkel, A. Merle, D. Meshcheriakov, H. Meyer, D. Milanesio, P. M. Cabrera, F. Monaco, M. Muraca, F. Nabais, V. Naulin, R. Nazikian, R. Nem, A. Nemes-Czopf, G. Neu, R. Neu, A. Nielsen, S. Nielsen, T. Nishizawa, M. Nocente, J.-M. Noterdaeme, I. Novikau, S. Nowak, M. Oberkofler, R. Ochoukov, J. Olsen, F. Orain, F. Palermo, O. Pan, G. Papp, I. P. Perez, A. Pau, G. Pautasso, C. Paz-Soldan, P. Petersson, P. Piovesan, C. Piron, U. Plank, B. Plaum, B. Plöck, V. Plyusnin, G. Pokol, E. Poli, L. Porte, T. Pütterich, M. Ramisch, J. Rasmussen, G. Ratta, S. Ratynskaia, G. Raupp, D. Réfy, M. Reich, F. Reimold, D. Reiser, M. Reisner, D. Reiter, T. Ribeiro, R. Riedl, J. Riesch, D. Rittich, J. R. Rodriguez, G. Rocchi, P. Rodriguez-Fernandez, M. Rodriguez-Ramos, V. Rohde, G. Ronchi, A. Ross, M. Rott, M. Rubel, D. Ryan, F. Ryter, S. Saarelma, M. Salewski, A. Salmi, O. Samoylov, L. S. Sanchez, J. Santos, O. Sauter, G. Schall, K. Schlüter, K. Schmid, O. Schmitz, P. Schneider, R. Schrittwieser, M. Schubert, C. Schuster, T. Schwarz-Selinger, J. Schweinzer, E. Seliunin, A. Shabbir, A. Shalpegin, S. Sharapov, U. Sheikh, A. Shevelev, G. Sias, M. Siccinio, B. Sieglin, A. Sigalov, A. Silva, C. Silva, D. Silvagni, J. Simpson, S. Sipilä, E. Smigelskis, A. Snicker, E. Solano, C. Sommariva, C. Sozzi, G. Spizzo, M. Spolaore, A. Stegmeir, M. Stejner, J. Stober, E. Strumberge, G. S. Lopez, H.-J. Sun, W. Suttrop, E. Sytova, T. Szepesi, B. Tál, T. Tala, G. Tardini, M. Tardocchi, D. Terranova, M. Teschke, E. Thorén, W. Tierens, D. Told, W. Treutterer, G. Trevisan, E. Trier, M. Tripský, M. Usoltceva, M. Valisa, M. Valovic, M. van Zeeland, F. Vannini, B. Vanovac, P. Varela, S. Varoutis, N. Vianello, J. Vicente, G. Verdoolaege, T. Vierle, E. Viezzer, I. Voitsekhovitch, U. von Toussaint, D. Wagner, X. Wang, M. Weiland, A. White, M. Willensdorfer, B. Wiringer, M. Wischmeier, R. Wolf, E. Wolfrum, Q. Yang, Q. Yu, R. Zagórski, I. Zammuto, T. Zehetbauer, W. Zhang, W. Zholobenko, M. Zilker, A. Zito, H. Zohm, S. Zoletnik, and t. EUROfusion MST1 Team, Nuclear Fusion **62**, 042006 (2022).

[15] S. J. Freethy, G. D. Conway, I. Classen, A. J. Creely, T. Happel, A. Köhn, B. Vanovac, and A. E. White, Review of Scientific Instruments **87**, 11E102 (2016).

[16] A. J. Creely, S. J. Freethy, W. M. Burke, G. D. Conway, R. Leccacorvi, W. C. Parkin, D. R. Terry, and A. E. White, Review of Scientific Instruments **89**, 053503 (2018).

[17] T. Happel, G. D. Conway, W. Kasparek, and B. Plaum, in *Proc. 10th Intl. Reflectometry Wksh. - IRW10* (Padova, 2011).

[18] O. Sauter and S.Yu. Medvedev, Computer Physics Communications **184**, 293 (2013).

[19] C. Holland, Physics of Plasmas **23**, 060901 (2016).

[20] P. W. Terry, M. Greenwald, J.-N. Leboeuf, G. R. McKee, D. R. Mikkelsen, W. M. Nevins, D. E. Newman, D. P. Stotler, Task Group on Verification and Validation, U.S. Burning Plasma Organization, and U.S. Transport Task Force, Physics of Plasmas **15**, 062503 (2008).

[21] G. M. Staebler, J. Candy, N. T. Howard, and C. Holland, Physics of Plasmas **23**, 062518 (2016).

[22] F. Jenko, W. Dorland, M. Kotschenreuther, and B. N. Rogers, Physics of Plasmas **7**, 1904 (2000).

[23] A. E. White, W. A. Peebles, T. L. Rhodes, C. H. Holland, G. Wang, L. Schmitz, T. A. Carter, J. C. Hillesheim, E. J. Doyle, L. Zeng, G. R. McKee, G. M. Staebler, R. E. Waltz, J. C. DeBoo, C. C. Petty, and K. H. Burrell, Physics of Plasmas **17**, 056103 (2010).

[24] S. J. Freethy, T. Görler, A. J. Creely, G. D. Conway, S. S. Denk, T. Happel, C. Koenen, P. Hennequin, A. E. White, and ASDEX Upgrade Team, Physics of Plasmas **25**, 055903 (2018).

[25] P. Schneider, A. Bustos, P. Hennequin, F. Ryter, M. Bernert, M. Cavedon, M. Dunne, R. Fischer, T. Görler, T. Happel, V. Igochine, B. Kurzan, A. Lebschy, R. McDermott, P. Morel, M. Willensdorfer, the ASDEX Upgrade Team, and The EUROfusion MST1 Team, Nuclear Fusion **57**, 066003 (2017).

[26] Y. Camenen, "Effect of isotope mass on transport and confinement: Overview of theoretical interpretations and current status of modelling," (2018).

[27] W. Horton, Reviews of Modern Physics **71**, 735 (1999).

[28] R. J. Fonck, G. Cosby, R. D. Durst, S. F. Paul, N. Bretz, S. Scott, E. Synakowski, and G. Taylor, Physical Review Letters **70**, 3736 (1993).

[29] J. G. Cordey, B. Balet, D. Campbell, C. D. Challis, J. P. Christiansen, C. Gormezano, C. Gowers, D. Muir, E. Righi, G. R. Saibene, P. M. Stubberfield, and K. Thomsen, Plasma Physics and Controlled Fusion **38**, A67 (1996).

[30] C. C. Petty, T. C. Luce, K. H. Burrell, S. C. Chiu, J. S. deGrassie, C. B. Forest, P. Gohil, C. M. Greenfield, R. J. Groebner, R. W. Harvey, R. I. Pinsker, R. Prater, R. E. Waltz, R. A. James, and D. Wròblewski, Physics of Plasmas **2**, 2342 (1995).

[31] P. Hennequin, Comptes Rendus Physique **7**, 670 (2006).

[32] G. Manfredi and M. Ottaviani, Physical Review Letters **79**, 4190 (1997).

[33] F. Chen, *Introduction to Plasma Physics and Controlled Fusion*, 3rd ed. (Springer Science+Business Media, New York, NY, 2015).

[34] T. S. Hahm and K. H. Burrell, Physics of Plasmas **2**, 1648 (1995).

[35] A. Bustos, A. Bañón Navarro, T. Görler, F. Jenko, and C. Hidalgo, Physics of Plasmas **22**, 012305 (2015).

[36] T. Hahm, L. Wang, W. Wang, E. Yoon, and F. Duthoit, Nuclear Fusion **53**, 072002 (2013).

[37] M. Nakata, M. Nunami, H. Sugama, and T.-H. Watanabe, Physical Review Letters **118**, 165002 (2017).

[38] J. Garcia, T. Görler, F. Jenko, and G. Giruzzi, Nuclear Fusion **57**, 014007 (2017).

[39] Y. Idomura, Physics of Plasmas **26**, 120703 (2019).

[40] E. A. Belli, J. Candy, and R. E. Waltz, Physical Review Letters **125**, 015001 (2020).

[41] N. Bonanomi, C. Angioni, P. Crandall, A. Di Siena, C. Maggi, P. Schneider, the ASDEX Upgrade Team, the EUROFusion MST1 Team, and JET Contributors, Nuclear Fusion **59**, 126025 (2019).

[42] R. Hawryluk, in *Physics of Plasmas Close to Thermonuclear Conditions* (Elsevier, 1981) pp. 19–46.

[43] D. Mc Cune, (1984).

[44] U. Plank, *The Effect of the Radial Electric Field around the Separatrix on the Access to the High Confinement Mode at ASDEX Upgrade*, Ph.D. thesis, Ludwig-Maximilians University, Munich (2021).

[45] B. Kurzan and H. D. Murmann, Review of Scientific Instruments **82**, 103501 (2011).

[46] E. Wolfrum, F. Aumayr, D. Wutte, Hp. Winter, E. Hintz, D. Rusbüldt, and R. P. Schorn, Review of Scientific Instruments **64**, 2285 (1993).

[47] N. A. Salmon, International Journal of Infrared and Millimeter Waves **15**, 53 (1994).

[48] E. Viezzer, T. Pütterich, R. Dux, R. M. McDermott, and ASDEX Upgrade Team, Review of Scientific Instruments **83**, 103501 (2012).

[49] R. M. McDermott, C. Angioni, R. Dux, E. Fable, T. Pütterich, F. Ryter, A. Salmi, T. Tala, G. Tardini, E. Viezzer, and the ASDEX Upgrade Team, Plasma Physics and Controlled Fusion **53**, 124013 (2011).

[50] R. Fischer, A. Bock, M. Dunne, J. C. Fuchs, L. Giannone, K. Lackner, P. J. McCarthy, E. Poli, R. Preuss, M. Rampp, M. Schubert, J. Stober, W. Suttrop, G. Tardini, M. Weiland, and ASDEX Upgrade Team, Fusion Science and Technology **69**, 526 (2016).

[51] R. Fischer, L. Giannone, J. Illerhaus, P. J. McCarthy, R. M. McDermott,

and ASDEX Upgrade Team, Fusion Science and Technology **76**, 879 (2020).
[52]R. Fischer, C. J. Fuchs, B. Kurzan, W. Suttrop, E. Wolfrum, and ASDEX Upgrade Team, Fusion Science and Technology **58**, 675 (2010).
[53]R. J. Groebner and T. H. Osborne, Physics of Plasmas **5**, 1800 (1998).
[54]A. Ho, J. Citrin, F. Auriemma, C. Bourdelle, F. Casson, H.-T. Kim, P. Manas, G. Szepesi, H. Weisen, and JET Contributors, Nuclear Fusion **59**, 056007 (2019).
[55]M. Hirsch, E. Holzhauer, J. Baldzuhn, and B. Kurzan, Review of Scientific Instruments **72**, 324 (2001).
[56]P. Hennequin, C. Honoré, A. Truc, A. Quéméneur, N. Lemoine, J.-M. Chareau, and R. Sabot, Review of Scientific Instruments **75**, 3881 (2004).
[57]T. Happel, A. B. Navarro, G. D. Conway, C. Angioni, M. Bernert, M. Dunne, E. Fable, B. Geiger, T. Görler, F. Jenko, R. M. McDermott, F. Ryter, U. Stroth, and the ASDEX Upgrade Team, Physics of Plasmas **22**, 032503 (2015).
[58]M. Bernert, T. Eich, A. Burckhart, J. C. Fuchs, L. Giannone, A. Kallenbach, R. M. McDermott, B. Sieglin, and ASDEX Upgrade Team, Review of Scientific Instruments **85**, 033503 (2014).
[59]J. Candy and R. E. Waltz, Physical Review Letters **91**, 045001 (2003).
[60]A. Cavallo and R. Cano, Plasma Physics **23**, 61 (1981).
[61]G. Cima, Review of Scientific Instruments **63**, 4630 (1992).
[62]J. Bendat and A. Piersol, *Random Data: Analysis and Measurement Procedures*, 1st ed. (John Wiley and Sons, Inc., 1971).
[63]S. Denk, R. Fischer, E. Poli, O. Maj, S. Nielsen, J. Rasmussen, M. Stejner, and M. Willensdorfer, Computer Physics Communications **253**, 107175 (2020).
[64]S. Denk, *Study of Non-Thermal Electron Energy Distribution Functions by Modeling of Electron Cyclotron Emission from the Fusion Plasmas at the ASDEX Upgrade Tokamak*, Ph.D. thesis, Technische Universitat Munchen, Munich (2018).
[65]D. E. Smith, E. J. Powers, and G. S. Caldwell, IEEE Transactions on Plasma Science **2**, 261 (1974).
[66]C. Watts, Fusion Science and Technology **52**, 176 (2007).
[67]R. J. Fonck, N. Bretz, G. Cosby, R. Durst, E. Mazzucato, R. Nazikian, S. Paul, S. Scott, W. Tang, and M. Zarnstorff, Plasma Physics and Controlled Fusion **34**, 1993 (1992).
[68]P. Hennequin, in *44th EPS Conference on Plasma Physics*, Vol. P1.167 (Belfast, UK, 2007).
[69]I. G. J. Classen, C. W. Domier, N. C. Luhmann, A. V. Bogomolov, W. Suttrop, J. E. Boom, B. J. Tobias, A. J. H. Donné, and ASDEX Upgrade Team, Review of Scientific Instruments **85**, 11D833 (2014).
[70]A. D. Piliya and A. Y. Popov, Plasma Physics and Controlled Fusion **44**, 467 (2002).
[71]I. H. Hutchinson, *Principles of Plasma Diagnostics*, 2nd ed. (Cambridge University Press, 2002).
[72]R. V. Bravenec and A. J. Wootton, Review of Scientific Instruments **66**, 802 (1995).
[73]J. E. Harvey, R. G. Irvin, and R. N. Pfisterer, Optical Engineering **54**, 035105 (2015).
[74]P. F. Goldsmith, Institute of Electrical and Electronics Engineers, and United Kingdom and Republic of Ireland Section, *Quasioptical Systems.* (Chapman & Hall, London, 1998).
[75]E. Poli, A. Peeters, and G. Pereverzev, Computer Physics Communications **136**, 90 (2001).
[76]E. Mazzucato, Review of Scientific Instruments **69**, 2201 (1998).
[77]M. Häse, M. Hirsch, and H. J. Hartfuss, Review of Scientific Instruments **70**, 1014 (1999).
[78]J. C. Hillesheim, W. A. Peebles, T. L. Rhodes, L. Schmitz, A. E. White, and T. A. Carter, Review of Scientific Instruments **81**, 10D907 (2010).
[79]J. C. Hillesheim, J. C. DeBoo, W. A. Peebles, T. A. Carter, G. Wang, T. L. Rhodes, L. Schmitz, G. R. McKee, Z. Yan, G. M. Staebler, K. H. Burrell, E. J. Doyle, C. Holland, C. C. Petty, S. P. Smith, A. E. White, and L. Zeng, Physics of Plasmas **20**, 056115 (2013).
[80]I. H. Hutchinson, Plasma Physics and Controlled Fusion **34**, 1225 (1992).
[81]T. L. Rhodes, W. A. Peebles, E. J. Doyle, P. Pribyl, M. Gilmore, R. A. Moyer, and R. D. Lehmer, Plasma Physics and Controlled Fusion **40**, 493 (1998).
[82]M. Gilmore, W. A. Peebles, and X. V. Nguyen, Plasma Physics and Controlled Fusion **42**, L1 (2000).
[83]E. Blanco, T. Estrada, and T. Happel, in *9th International Reflectometry Workshop (IRW9) for Fusion Plasma Diagnostics* (Lisbon, Portugal, 4th to 6th of May 2009).
[84]G. D. Conway, Plasma Physics and Controlled Fusion **39**, 407 (1997).
[85]E. Z. Gusakov and A. Y. Popov, Plasma Physics and Controlled Fusion **44**, 2327 (2002).
[86]S. Freethy, C. Lechte, P. Rodriguez-Fernandez, E. Fable, T. Goerler, T. Happel, P. Hennequin, and A. E. White, in *14th International Reflectometry Workshop - IRW14* (Lausanne, Switzerland, 2019) p. O.305.
[87]J. Breslau, M. Gorelenkova, F. Poli, J. Sachdev, and X. Yuan, "TRANSP," Princeton Plasma Physics Laboratory (PPPL), Princeton, NJ (United States) (2018).
[88]Braginskii, Reviews of Plasma Physics **1**, 205 (1965).
[89]F. Porcelli, D. Boucher, and M. N. Rosenbluth, Plasma Physics and Controlled Fusion **38**, 2163 (1996).
[90]Y. Idomura and M. Nakata, Physics of Plasmas **21**, 020706 (2014).
[91]G. M. Staebler, J. E. Kinsey, and R. E. Waltz, Physics of Plasmas **12**, 102508 (2005).
[92]G. M. Staebler, J. E. Kinsey, and R. E. Waltz, Physics of Plasmas **14**, 055909 (2007).
[93]G. M. Staebler, J. Candy, E. A. Belli, J. E. Kinsey, N. Bonanomi, and B. Patel, Plasma Physics and Controlled Fusion **63**, 015013 (2021).
[94]G. Staebler, E. A. Belli, J. Candy, J. Kinsey, H. Dudding, and B. Patel, Nuclear Fusion **61**, 116007 (2021).
[95]G. Staebler, J. Candy, R. Waltz, J. Kinsey, and W. Solomon, Nuclear Fusion **53**, 113017 (2013).
[96]Turbulence and Transport group, "Plasma Rotation," http://gafusion.github.io/doc/rotation.html (2023).
[97]A. J. Creely, P. Rodriguez-Fernandez, G. D. Conway, S. J. Freethy, N. T. Howard, A. E. White, and the ASDEX Upgrade Team, Plasma Physics and Controlled Fusion **61**, 085022 (2019).
[98]T. Görler, A. E. White, D. Told, F. Jenko, C. Holland, and T. L. Rhodes, Physics of Plasmas **21**, 122307 (2014).
[99]J. C. Hillesheim, W. A. Peebles, T. L. Rhodes, L. Schmitz, T. A. Carter, P.-A. Gourdain, and G. Wang, Review of Scientific Instruments **80**, 083507 (2009).
[100]P. Rodriguez-Fernandez, A. E. White, A. J. Creely, M. J. Greenwald, N. T. Howard, F. Sciortino, and J. C. Wright, Fusion Science and Technology **74**, 65 (2018).
[101]C. Holland, A. E. White, G. R. McKee, M. W. Shafer, J. Candy, R. E. Waltz, L. Schmitz, and G. R. Tynan, Physics of Plasmas **16**, 052301 (2009).
[102]G. H. Hammett, W. Dorland, N. F. Loueiro, and T. Tatsuno, in *APS Division of Plasma Physics Meeting* (Philadelphia, 2006).
[103]B. F. McMillan, J. Ball, and S. Brunner, Plasma Physics and Controlled Fusion **61**, 055006 (2019).
[104]D. Told, *Gyrokinetic Microturbulence in Transport Barriers*, Ph.D. thesis, Universität Ulm (2012).
[105]A. Lebschy, *Experimental Characterization of the Core Plasma Flow at the ASDEX Upgrade Tokamak*, Ph.D. thesis, Technische Universität München, Munich, Germany (2018).
[106]A. Lebschy, R. McDermott, C. Angioni, B. Geiger, D. Prisiazhniuk, M. Cavedon, G. Conway, R. Dux, M. Dunne, A. Kappatou, T. Pütterich, U. Stroth, E. Viezzer, and the ASDEX Upgrade Team, Nuclear Fusion **58**, 026013 (2018).
[107]W. A. Houlberg, K. C. Shaing, S. P. Hirshman, and M. C. Zarnstorff, Physics of Plasmas **4**, 3230 (1997).
[108]P. R. Bevington and D. K. Robinson, *Data Reduction and Error Analysis for the Physical Sciences*, 3rd ed. (McGraw-Hill, Boston, 2003).
[109]B. Efron and R. Tibshirani, *An Introduction to the Bootstrap*, Monographs on Statistics and Applied Probability No. 57 (Chapman & Hall, New York, 1993).
[110]X. Garbet, Y. Idomura, L. Villard, and T. Watanabe, Nuclear Fusion **50**, 043002 (2010).
[111]M. Greenwald, Physics of Plasmas **17**, 058101 (2010).
[112]P. Ricci, C. Theiler, A. Fasoli, I. Furno, K. Gustafson, D. Iraji, and J. Loizu, Physics of Plasmas **18**, 032109 (2011).
[113]A. Snicker, E. Poli, O. Maj, L. Guidi, A. Köhn, H. Weber, G. Conway, M. Henderson, and G. Saibene, Nuclear Fusion **58**, 016002 (2018).
[114]W. A. Gardner, Signal Processing **29**, 113 (1992).

[115]C. Lechte, G. D. Conway, T. Görler, T. Happel, and the ASDEX Upgrade Team, Plasma Science and Technology **22**, 064006 (2020).
[116]S. J. Freethy, T. Görler, A. J. Creely, G. D. Conway, S. S. Denk, T. Happel, P. Henniquin, C. Koenen, A. E. White, and ASDEX Upgrade team, EPJ Web of Conferences **203**, 03001 (2019).
[117]P. Molina Cabrera, S. Coda, L. Porte, A. Smolders, and TCV Team, Review of Scientific Instruments **90**, 123501 (2019).
[118]O. Krutkin, S. Brunner, and S. Coda, Submitted (2023).
[119]C. Sung, A. White, N. Howard, C. Oi, J. Rice, C. Gao, P. Ennever, M. Porkolab, F. Parra, D. Mikkelsen, D. Ernst, J. Walk, J. Hughes, J. Irby, C. Kasten, A. Hubbard, M. Greenwald, and the Alcator C-Mod Team, Nuclear Fusion **53**, 083010 (2013).